Journal of Building Engineering 128 (2026) 116654

Contents lists available at ScienceDirect

Journal of Building Engineering

journal homepage: www.elsevier.com/locate/jobe

The influence of metakaolin-to-vaterite ratio on the properties of vaterite-calcined clay cement: fresh mortar rheology, microstructure, and mechanical performance

Mohammad Hossein Nofalah, Loucas Kyriakou, José María Fernández, Íñigo Navarro-Blasco, José Ignacio Álvarez *

MATCH Research Group, Department of Chemistry, School of Sciences, University of Navarra, C/. Irunlarrea 1, Pamplona, 31008, Spain

A B S T R A C T

This study investigates the influence of the metakaolin-to-vaterite (MK/V) ratio on the fresh properties, mechanical performance, and microstructural development of vaterite-calcined clay cement (VC^3) mortars. Eight mixtures were produced with MK/V ratios between 1.0 and 3.0, alongside a limestone-calcined clay cement (LC^3) reference. Fresh- and hardened-state behaviors were assessed using flow-table testing, rheological characterization, setting-time measurements, isothermal calorimetry, compressive strength testing, thermogravimetric analysis, X-ray diffraction, and scanning electron microscopy. Replacing calcite with vaterite enhanced flowability and reduced both static and dynamic yield stresses due to the spherical morphology of vaterite. Increasing metakaolin content, however, progressively elevated yield stresses and thixotropy. Vaterite addition slightly prolonged setting time relative to LC^3 due to the high surface-related adsorption capacity of vaterite for calcium and sulfate ions, although higher MK/V ratios accelerated hydration and offset this delay. Early-age compressive strengths were comparable to LC^3, while all VC^3 mixtures exceeded LC^3 performance after 7 days. Strength increased with MK/V ratio up to an optimum range of 2.0-2.5, where a maximum improvement of 42% at 91 days was recorded. Thermogravimetric and XRD analyses showed efficient portlandite consumption and the formation of a multiphase assemblage dominated by C-(A)-S-H and AFm-type carboaluminate phases. SEM-EDS confirmed the development of a dense, chemically complex matrix underpinning the superior strength performance. Overall, the MK/V ratio was found to regulate the interplay between rheology, hydration, and microstructure, identifying 2.0-2.5 as the optimal range for balanced performance. Given that vaterite can be produced via carbon-negative synthesis routes that permanently store captured CO_2, ternary samples including metakaolin emerge as a technically robust and environmentally beneficial alternative for next-generation low-clinker cements.

1. Introduction

The industrial use of natural carbonate minerals, particularly in cement, paper, plastic, and rubber, has significantly contributed to anthropogenic carbon dioxide (CO_2) emissions [1,2]. Although these minerals serve as long-term geological reservoirs of CO_2, their extraction and thermal processing release substantial quantities of CO_2, disrupting the natural carbon cycle [3].

Among these sectors, the cement industry is the most significant contributor to CO_2 emissions originating from carbonate decomposition, accounting for approximately 8% of global anthropogenic CO_2 emissions. With annual production surpassing 4 billion tons, cement manufacturing emits more than 1.6 billion metric tons of CO_2 each year, and demand is projected to rise by 50% by 2050 [1,4]. This considerable carbon footprint underscores the urgent need for strategies to reduce the carbon intensity of cementitious materials [5].

A major mitigation pathway involves the partial substitution of Portland cement clinker with supplementary cementitious

* Corresponding author.
E-mail address: jalvarez@unav.es (J.I. Álvarez).

https://doi.org/10.1016/j.jobe.2026.116654
Received 4 February 2026; Received in revised form 5 June 2026; Accepted 15 June 2026
Available online 16 June 2026

materials (SCMs). These include naturally occurring pozzolans such as volcanic ash and trass [6,7], as well as industrial by-products like fly ash, ground granulated blast furnace slag, and silica fume [8–12]. The development of alkali-activated binders and cement-free concrete systems has further expanded the role of SCMs in sustainable cement chemistry [13,14]. While these approaches successfully reduce clinker content without compromising performance, the global supply of common SCMs may be insufficient to meet future demand, highlighting the need to explore alternative materials [15].

Calcium carbonate has been effectively incorporated into blended cements such as slag-limestone [16] and fly ash-limestone systems [17], contributing to greener construction materials. Among these, limestone-calcined clay cement (LC^3) has gained particular prominence due to its strong balance of reactivity, global availability, and environmental benefits [18]. In these systems, calcined clay provides reactive alumina, while calcium carbonate promotes the formation of carboaluminates, such as hemicarboaluminate (Hc) and monocarboaluminate (Mc) [19], and acts as a nucleation site for calcium silicate hydrate (C-S-H) precipitation [20]. These synergistic effects support strength development and microstructural refinement, enabling LC^3 to match or even exceed the performance of ordinary Portland cement (OPC) [21–24] while reducing CO_2 emissions by up to 40% [21].

Most research has focused on calcite, the thermodynamically stable polymorph of calcium carbonate. However, metastable polymorphs, particularly vaterite, possess distinct physicochemical properties that may enhance the performance of ternary binders [22,25,26], yet remain relatively underexplored. Vaterite can be synthesized from calcium-rich industrial by-products such as recycled concrete fines [26], basic oxygen furnace slag [27], carbide sludge [28], and magnesium slag [29] via controlled carbonation processes that utilize CO_2 captured from ambient air or point-source emissions [30]. This production route provides dual sustainability benefits: valorization of calcium-based waste and atmospheric CO_2 capture. Recent advances in mineralization technologies have enabled cost-effective, scalable vaterite production, with potential net-negative emissions of approximately 0.14 kg CO_2 per kilogram of vaterite, depending on process configuration and energy source [20].

Despite these advantages, relatively few studies have assessed vaterite as a supplementary cementitious material [5,25,26,31,32], and the systems investigated have typically involved sulfoaluminate cements, mixes containing recycled aggregates, or formulations designed for waste incorporation. Only two studies have examined vaterite in LC^3-type systems [22], including thus a calcined clay, like MK, leaving significant gaps in understanding.

However, the fundamental behavior of VC^3 remains insufficiently characterized. Critical questions remain regarding how MK in combination with vaterite content affects hydration kinetics, phase assemblage, pore structure, and the resulting mechanical and rheological properties. Moreover, rheological parameters, for instance static and dynamic yield stress and thixotropy, have not been systematically investigated, despite their importance for advanced processes such as 3D printing and pumped construction.

To address these gaps, eight mixtures were designed, including seven VC^3 mixtures with varying metakaolin-to-vaterite (MK/V) ratios and an LC^3 control. Given that conventional LC^3 systems are thoroughly documented in the literature, the LC^3 mixture here serves strictly as a synchronized experimental baseline to isolate and highlight the specific physicochemical impacts of the synthesized vaterite polymorph. Fresh-state behavior was evaluated through flowability, yield stress, and thixotropy; mechanical performance was assessed through compressive strength at 3, 7, 28, and 91 days; and hydration and microstructure were characterized using isothermal calorimetry, X-ray diffraction (XRD), thermogravimetric analysis (TGA), and scanning electron microscopy (SEM).

The results clarify the performance of these vaterite-calcined clay (VC^3) binding systems, elucidate the mechanisms controlling VC^3 performance, and demonstrate its potential as a technically viable and environmentally advantageous alternative to conventional LC^3 systems.

2. Materials and methods

2.1. Materials

The materials used in this study included a CEM I 52.5 R cement (CE and NF certified), supplied by Grupo Cementos Portland Valderrivas. As calcined clay, metakaolin (Metaver N), provided by NEWCHEM, was used. Calcium carbonate in the form of calcite (CACB-00 A) and gypsum (CASU-02 A), both with purities exceeding 99%, were obtained from Labkem. Standardized CEN sand, conforming to EN 196-1 specifications [33], was used for preparing all mortar mixtures.

Vaterite was synthesized in the laboratory through a controlled precipitation procedure, achieving a purity of 98 ± 2%. The synthesis method followed the procedure reported in a previous study by our research group [34]. Table 1 summarizes the chemical composition and physical properties of the raw materials and Table 2 presents the crystalline phases composition of OPC, while Fig. 1

Table 1
Chemical composition and physical characteristics of the raw materials (wt.%).

Raw material	CaO (%)	SiO_2 (%)	Al_2O_3 (%)	Fe_2O_3 (%)	K_2O (%)	Na_2O (%)	MgO (%)	SO_3 (%)	LOI[a] (%)	Dv, 10 (μm)	Dv, 50 (μm)	Dv, 90 (μm)
Cement	68.8	16.0	5.0	2.1	1.1	0.2	1.8	3.8	2.8	0.3	11.3	26.4
Metakaolin	0.3	45.9	48.6	0.9	0.9	1.0	1.7	n.d.	0.9	0.3	2.5	11.3
Gypsum	40.6	2.0	1.2	n.d.	0.1	n.d.	1.6	52.4	21.2	10.5	41.7	89.4
Calcite	55.2	0.3	n.d.	n.d.	0.1	n.d.	0.1	n.d.	44.8	0.2	2.9	4.9
Vaterite	54.3	0.3	n.d.	n.d.	0.8	n.d.	0.1	n.d.	46.0	0.3	9.1	17.9

[a] LOI: Loss of ignition, determined by thermogravimetric analysis; n.d.: not detected.

shows their particle size distributions (PSD). Scanning electron microscopy images of the synthesized vaterite are provided in Fig. 3, and its morphology and particle size as observed by transmission electron microscopy (TEM) are presented in Fig. 4. The crystalline phases of the calcium carbonate materials, identified using X-ray diffraction, are illustrated in Fig. 2.

A polycarboxylate ether (PCE)-based superplasticizer (MasterCast GT 205), supplied in powder form, was added into all mixtures. The admixture has a density of 0.870-0.970 g/cm^3 and an average molecular weight of approximately 8000 g/mol.

Fig. 1 presents the particle size distribution (PSD) of the binders. Metakaolin displays a relatively broad distribution, dominated by particles in the 2–5 μm range, with a maximum volume fraction of about 5.2 at 4.5 μm and a gradual decline thereafter. Cement particles fall within a narrower and finer range, with the highest volume concentration between 8 and 20 μm. Gypsum, in contrast, is the coarsest of the raw materials, showing its peak between 40 and 70 μm and negligible fractions below 0.8 μm. Both calcium carbonate powders contain a notable fraction of particles below 1 μm, with the volume concentration rising from approximately 0.01 at 0.05 μm. Vaterite shows a broader distribution with a local maximum between 10 and 15 μm, whereas calcite reaches its peak between 3 and 5 μm. These differences in size distribution account for the distinct specific surface areas measured for the calcium carbonates. BET surface area measurements obtained from N_2 adsorption yielded values of 14.55 m^2/g for calcite and 7.52 m^2/g for vaterite. Scanning electron microscopy and transmission electron microscopy (TEM) images (Figs. 3 and 4) show that vaterite particles predominantly exhibit a spherical and porous morphology. TEM observations indicate an average primary particle size of approximately 75 nm; however, these primary particles display a pronounced tendency to agglomerate (Figs. 3c and 4a), forming secondary spherical aggregates. These secondary vaterite spheres further cluster together, as illustrated in Figs. 3a and 4b. The particle size values obtained by laser diffraction (Fig. 1) reflect this secondary agglomeration behavior.

These findings are consistent with previous studies reporting the coexistence of primary nanoscale vaterite particles and their secondary spherical aggregates, as well as their strong agglomeration tendency [35]. The characterization results in this study align well with established literature, including the size range of primary and secondary particles, the D_{50} value of the PSD, the surface roughness of the spheres, and the measured specific surface area [28,35–37].

X-ray diffraction patterns (Fig. 2) confirm the successful synthesis of vaterite with high phase purity, showing it as the dominant phase with only trace amounts of calcite. TGA provided loss on ignition (LOI) values of 44.8% for calcite and 46.0% for vaterite. These values are in good agreement with the theoretical CO_2 content of pure calcium carbonate, fully decomposed near 800 °C, and further support the high purity of both carbonate powders (Table 1).

The mineralogical analysis of the MK revealed that mullite (PDF-2 file 82-0037) was the main mineralogical component (ca. 50%), followed by corundum (PDF 46-1212) (ca. 25%), and 22-24% of phases of SiO_2, as quartz (PDF 70-3755) and cristobalite (89-3607). The MK morphology and particle size are presented in Figs. 5 and 6, as observed by SEM and TEM.

2.2. Methods

2.2.1. Vaterite synthesis

Vaterite was synthesized in the laboratory following the controlled aqueous precipitation procedure previously reported in our research [34]. First, a 4 M potassium carbonate (K_2CO_3) solution was prepared using distilled water. Separately, a mixed 2 M solution of calcium chloride ($CaCl_2$) and ammonium chloride (NH_4Cl) was prepared in distilled water. The K_2CO_3 solution was then rapidly added to the $CaCl_2$-NH_4Cl solution at a 2:1:1 M ratio (K_2CO_3:$CaCl_2$:NH_4Cl) under continuous stirring at 600 rpm. Stirring was maintained for 10 min to ensure complete precipitation of calcium carbonate.

The resulting suspension was immediately filtered using a Büchner funnel with filter paper to recover the solid precipitate. The collected solid was washed with a small amount of distilled water, followed by 70% ethanol to prevent further crystallization and phase transformation. Finally, the product was dried in an oven at 80 °C for 24 h.

2.2.2. Characterization of raw materials: X-ray fluorescence (XRF), particle size distribution, and specific surface area

The chemical composition of the raw materials, summarized in Table 1, was determined via X-ray fluorescence (XRF) using a Bruker S2 Puma spectrometer (Bruker Scientific Instruments, Billerica, MA, USA). Measurements were conducted under a helium atmosphere with a 4 μm polypropylene filter and an X-ray tube equipped with a silver anode. Quantitative analyses were performed using Spectra Results Manager software (Bruker AXS Spectra Elements v2.3).

Particle size distribution was measured by laser diffraction using a Malvern Mastersizer (Malvern Panalytical Ltd., Malvern, UK). Suspensions were prepared at 10% wt./wt. In distilled water.

Specific surface area was assessed by nitrogen adsorption according to the Brunauer-Emmett-Teller (BET) method, using a Micromeritics ASAP 2020 Surface Area and Porosity Analyzer (Micromeritics Instrument Corp., Norcross, GA, USA). Approximately 0.2-0.3 g of sample was degassed under vacuum, first at 90 °C for 1 h and then at 200 °C for 4 h, using a heating rate of 10 °C/min. Nitrogen adsorption was carried out at −196 °C within a relative pressure range (P/P_0) of 0.05-0.30, and surface area values were calculated using the instrument's dedicated software (ASAP 2020 V^4.00).

Table 2
Crystalline phases proportion of OPC.

C_3S	C_2S	C_3A	C_4AF	Gypsum	Dolomite	Periclase
60.4	16.3	12.5	3.0	4.1	1.2	2.1

C = CaO, S = SiO_2, A = Al_2O_3, F = Fe_2O_3.

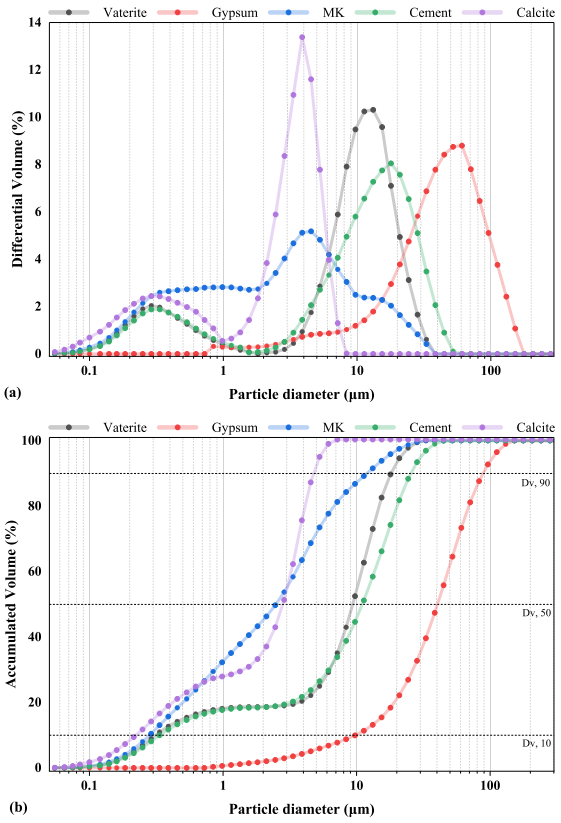

Fig. 1. Particle size distribution of the raw materials obtained by laser diffraction: (a) differential volume distribution and (b) cumulative volume distribution.

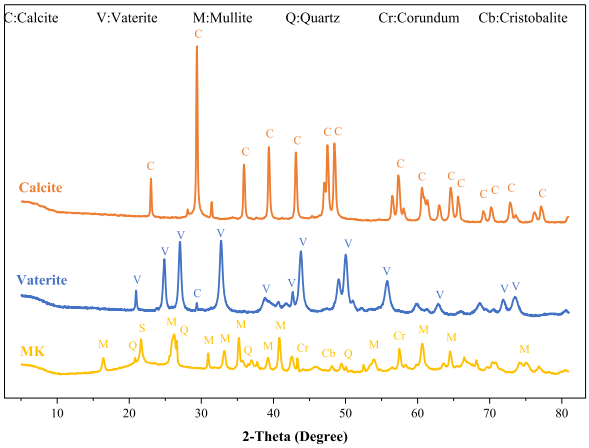

Fig. 2. X-ray diffraction patterns of the metakaolin, calcite, and vaterite polymorphs.

2.2.3. Mortar preparation

Eight mortar mixtures were prepared in total: seven VC^3 mixtures and one LC^3 mortar, which served as the control. All mixtures were formulated with a constant water-to-binder ratio (w/b) of 0.5 and a sand-to-binder ratio of 3:1 by weight. The primary objective was to assess the influence of MK/V ratio on the VC^3 mixtures, with the LC^3 reference mortar providing a baseline for comparison.

This standardized mix-design methodology enabled direct evaluation of the MK/V ratio on both fresh and hardened mortar properties. Table 3 presents the detailed mix proportions and material compositions for all mortars and pastes.

For the preparation of the fresh mortars, the dry components (standard sand, metakaolin, gypsum, calcite, vaterite, and

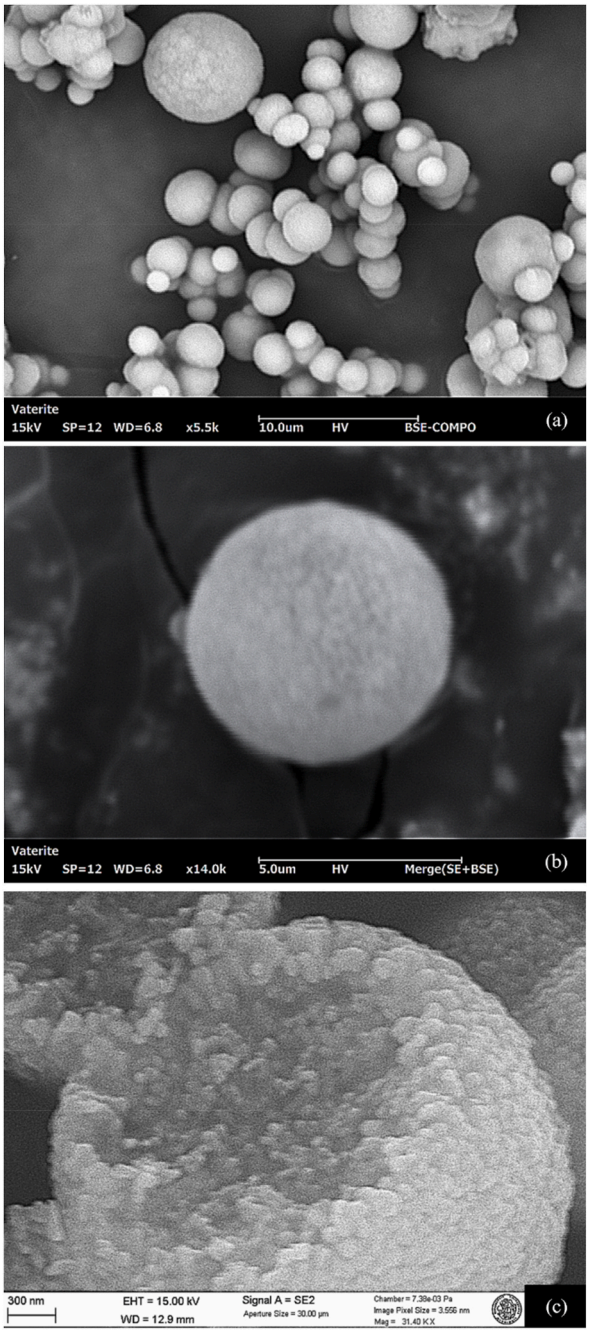

Fig. 3. SEM micrographs of the synthesized vaterite showing particle morphology and size at different magnifications: (a) BSE image at 5500×, (b) merged SE + BSE image at 14,000x, and (c) SE image at 31,400x.

superplasticizer) were first blended in a solid-additives mixer (Model BL-8-CA, Lleal, S.A., Granollers, Spain) for 5 min to ensure homogeneity. Water was then gradually added and mixed at low speed for more than 270 s using a Proeti ETI 26.0072 mixer (Proeti, Madrid, Spain). The fresh mortars were subsequently cast into cylindrical PVC molds (Ø = 30 mm, h = 40 mm), following the procedure established in previous studies [38]. Specimens were cured in a climatic chamber at 95 ± 5% relative humidity and 20 ± 2 °C for up to 91 days.

Compressive strength was measured on three specimens at each curing age to ensure reproducibility and statistical reliability. Additionally, one specimen per curing age was freeze-dried to halt ongoing carbonation and hydration processes and then analyzed by X-ray diffraction, thermogravimetric analysis, and microstructural techniques. The freeze-drying procedure involved immersion in liquid N_2 for 5 min, followed by sublimation at −40 °C under a 1 Pa vacuum for 24 h, effectively preserving the mortar microstructure

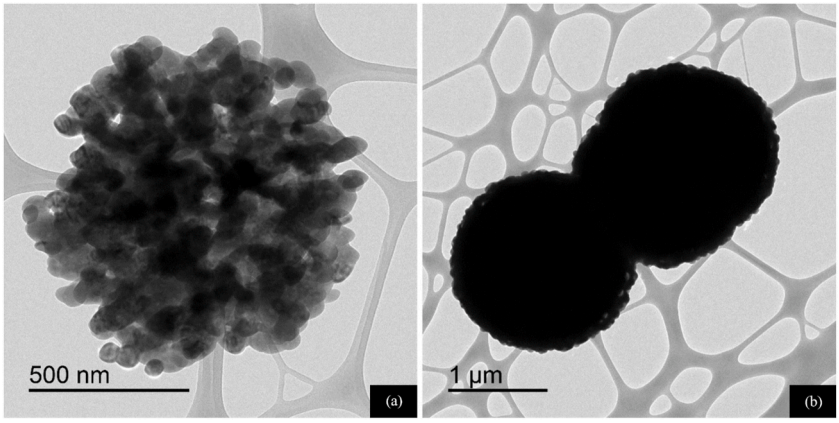

Fig. 4. TEM micrographs of the synthesized vaterite particles illustrating their morphology and size: (a) porous structure and agglomeration of individual primary particles, and (b) morphology and agglomeration of secondary spherical aggregates.

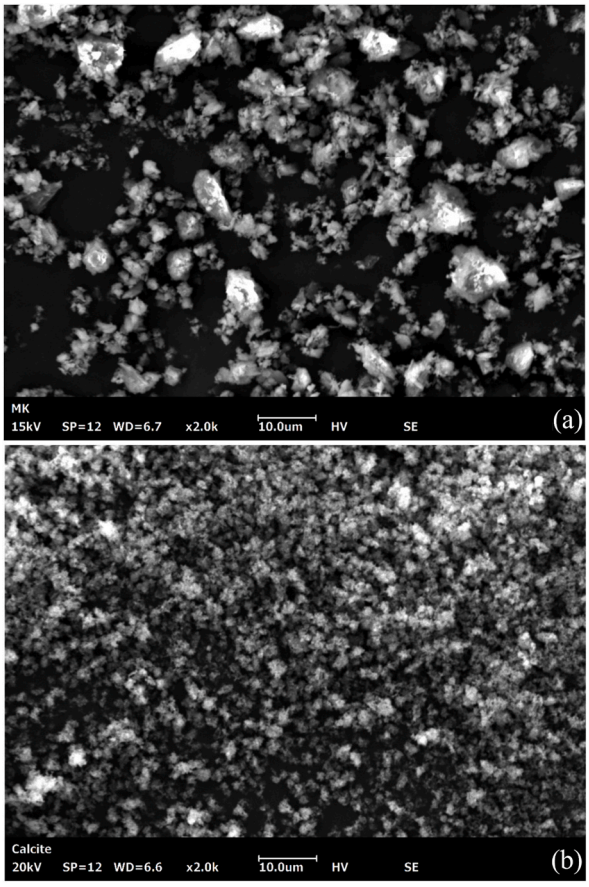

Fig. 5. SEM micrographs of the MK and calcite particle morphology: (a) MK, (b) calcite.

[39].

2.2.4. *Fresh state tests*

Workability was evaluated using the flow table test in accordance with UNE-EN 1015-3 [40]. Fresh mortar was placed into a truncated cone mold (100 mm base diameter, 70 mm top diameter, and 60 mm height) in two layers, each compacted with a tamping rod. After removing the mold, the flow table was dropped 15 times at a constant frequency to allow the mortar to spread, and the

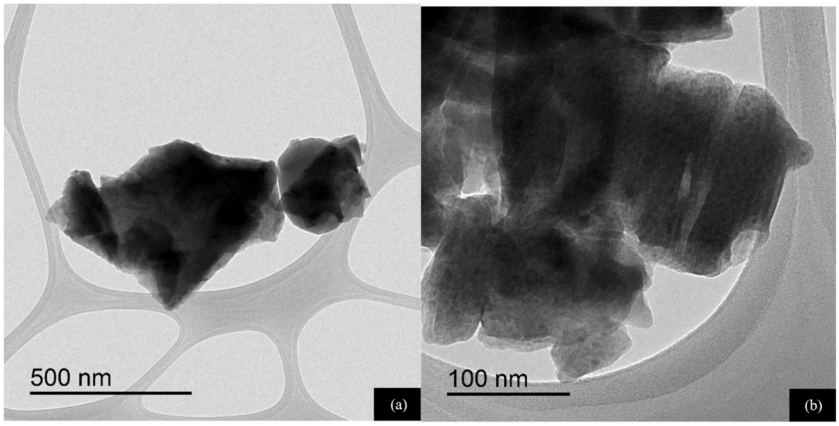

Fig. 6. Metakaolin particles TEM micrographs indicating (a) size, and (b) angular morphology.

Table 3
Mix proportions of mortar mixtures (weight percentage of binder components).

Name	Binder					MK/V	PCE (%)	Water/Binder	Sand/Binder
	Cement (%)	MK (%)	V (%)	C (%)	G (%)				
LC^3	50	30.0	-	15	5	-	0.2	0.5	3
VC^3-1	50	22.5	22.5	-	5	1.00	0.2	0.5	3
VC^3-1.5	50	27.0	18.0	-	5	1.50	0.2	0.5	3
VC^3-1.75	50	28.6	16.4	-	5	1.75	0.2	0.5	3
VC^3-2	50	30.0	15.0	-	5	2.00	0.2	0.5	3
VC^3-2.25	50	31.2	13.8	-	5	2.25	0.2	0.5	3
VC^3-2.5	50	32.2	12.8	-	5	2.50	0.2	0.5	3
VC^3-3	50	33.8	11.2	-	5	3.00	0.2	0.5	3

MK = Metakaolin, V = Vaterite, C = Calcite, G = Gypsum.

resulting diameter was measured to quantify workability.

Setting times were determined following UNE-EN 1015-9 [41] by measuring resistance to penetration at fixed intervals after mixing until a value of 0.5 N/mm^2 was reached, which was taken as the limit of the workable period prior to the onset of setting.

The rheological behavior of the mortars was assessed using a HAAKE Viscotester VT 550, determining the static yield stress at two low shear rates ($\dot{\gamma} = 0.05\ s^{-1}$ and 0.5–1 s^{-1}), the dynamic yield stress, and the thixotropy. The static yield stress measured at $\dot{\gamma} = 0.05\ s^{-1}$ reflects the minimum stress required to initiate flow under very gentle deformation, representing the strength of the undisturbed microstructure. Measurements at slightly higher shear rates ($0.5 < \dot{\gamma} < 1\ s^{-1}$) capture the material's resistance as flow begins but before complete structural breakdown. Dynamic yield stress was determined by gradually decreasing the shear rate from 4 s^{-1} to 0.5 s^{-1} and fitting the resulting steady flow curve to the Bingham model. Thixotropy was evaluated via cyclic shear tests, where alternating low and high shear rates were applied; the thixotropy index was calculated from the area of the hysteresis loop in the stress-shear rate curve.

2.2.5. Isothermal calorimetry

Hydration kinetics were monitored using an 8-channel TAM Air isothermal calorimeter (TA Instruments) operating at 25 °C for 3 days with ±0.15 °C temperature accuracy and temperature stability at ±0.001 °C. Paste samples (20 g) were prepared by mixing distilled water with the binders (Table 3) using a vertical-axis high-shear blender at 1600 rpm for 2 min. The fresh pastes were sealed in glass ampoules and immediately placed into the calorimeter for testing.

2.2.6. Mechanical performance

Compressive strength was measured at 3, 7, 28, and 91 days using a Frank/Controls 81,565 press equipped with a Proeti ETI 26.0052 (capacity: 5000 kg). Cylindrical specimens were tested according to ASTM C39, applying a loading rate between 5 and 50 kP/s [42]. All compressive strength values are reported as the mean of three replicate specimens, with the calculated standard deviation explicitly displayed as error bars to illustrate data dispersion.

2.2.7. Sustainability indicator

The development of eco-efficient construction materials requires minimizing environmental impact while maintaining adequate performance. To evaluate both aspects simultaneously, a Sustainability Indicator (S_i) was computed to compare the environmental efficiency of the different mixtures. S_i was defined as the ratio between the CO_2 emissions associated with 100 kg of binder solids and

the 91-day compressive strength of the corresponding mortar (Eq. (1)). A lower S_i value indicates a more sustainable mixture. In any case, this indicator should be regarded strictly as a simplified comparative estimation. Notably, this exact screening approach was utilized by Sun et al. [21] to compare low-clinker LC^3 formulations against standard reference matrices using literature-derived carbon baselines.

The laboratory synthesis route was strictly optimized for phase purity to ensure maximum experimental repeatability and reproducibility, as the primary objective of this study was to characterize the fundamental material properties and hydration mechanisms of the resulting blended matrices. This controlled bench-scale approach was necessary to cleanly isolate the fundamental hydration kinetics of the novel VC^3 matrix. By eliminating uncontrolled mineralogical impurities, the physical-chemical behavior of the fresh and hardened states could be accurately characterized without confounding variables. Consequently, this method establishes a reliable material baseline, leaving economic and environmental manufacturing optimization to separate industrial scaling frameworks.

The CO_2 emissions associated with cement [43], calcined clay [43], calcite [43], gypsum [43], and vaterite [22] were estimated using published life cycle assessment (LCA) data.

$$S_i\left(\frac{kgCO_2}{MPa}\right) = \frac{CO_2\ emissions/100\ kg\ of\ solids}{91-day\ compressive\ strength} \quad \text{(Eq.1)}$$

2.2.8. Thermogravimetric analysis

Thermogravimetric analysis was conducted using a TA Instruments SDT650 (New Castle, DE, USA), with data processed in TRIOS software. Approximately 10 mg of each sample was placed into 90 μL alumina crucibles and heated from 35 °C to 1100 °C at 20 °C/min under a nitrogen atmosphere (flow rate 100 mL/min). Interpretation of mass-loss events followed established literature guidelines [44, 45].

2.2.9. XRD quantitative phase analysis (QPA)

Phase identification of powdered samples were performed using a Bruker D8 Advance diffractometer (Bruker Scientific Instruments, Billerica, MA, USA) equipped with Cu $K\alpha_1$ radiation. Scans were collected over a 2θ range of 5°-80°, with a step size of 0.03° and a counting time of 1 s per step. The paste mixtures were prepared following the proportions listed in Table 3, but sand was omitted in order to eliminate the strong quartz reflections that would otherwise dominate the diffraction signal. The samples were ground to a particle size below 5 μm to reduce preferred orientation and ensure reliable quantification.

Diffractograms were processed using Diffrac.EVA software (version 4.3.0.1, Bruker AXS) for the qualitative identification of crystalline phases. Rietveld refinement was carried out with TOPAS v.6 to quantify the crystalline phases present at various hydration ages. For quantitative phase analysis, 10 wt% corundum (Al_2O_3) was added to each powdered sample as an internal reference. The absolute weight fractions for all detected crystalline phases were enabled with the corundum internal standard.

2.2.10. Microstructural studies: scanning/transmission electron microscopy (SEM/TEM)

Microstructural characterization was performed using two scanning electron microscopes: a COXEM EM-30N (COXEM Co., Ltd., Daejeon, Republic of Korea) and a ZEISS Sigma 300 VP FE-SEM. Fractured mortar surfaces were mounted on stubs using silver paste or carbon tape, then gold-coated with a COXEM SPT-20 Ion Coater (COXEM Co., Ltd., Daejeon, Republic of Korea) at 4 mA for 120 s. Both secondary electron (SE) and backscattered electron (BSE) imaging modes were employed to document surface morphology and contrast mineralogical features. Elemental composition was analyzed with a Quantax Compact 30 Bruker EDS detector (Bruker Nano GmbH, Berlin, Germany), and spectra were processed using Esprit Compact software (version 2.3.1.1019, Bruker).

Transmission electron microscopy (TEM) was performed on a JEOL JEM-1400 Plus operating at 120 kV and equipped with an

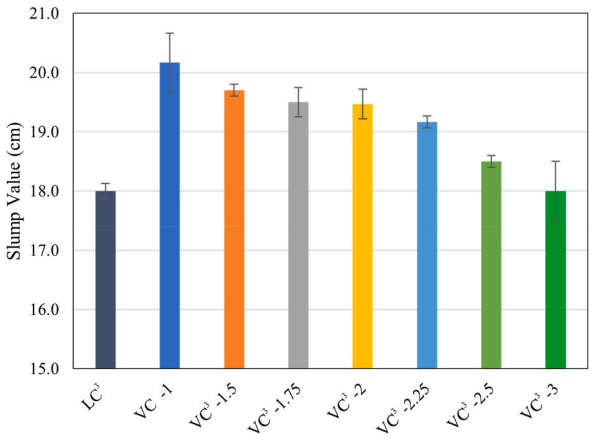

Fig. 7. Flowability of the mortar mixtures determined according to the UNE-EN 1015-3 standard.

ORIUS GATAN SC600 camera. Images were processed using DigitalMicrograph 1.80.70 within the Gatan Microscopy Suite (GMS) version 1.8.0.

3. Results and discussion

3.1. Workability (flow-table test) and mortar rheology

Fig. 7 shows the results of the flow table test, which provide insight into the fluidity of the different mortar mixtures. As previously reported, LC^3 mortars exhibit lower fluidity than OPC-based mixtures [22], confirming that a reduction in OPC content typically leads to decreased workability. In contrast, the VC^3 mixtures demonstrated higher fluidity than the LC^3 control, indicating that the incorporation of vaterite has a positive effect on fresh-state properties.

Within the VC^3 series, however, an increase in the metakaolin-to-vaterite (MK/V) ratio resulted in a gradual reduction in slump values. This behavior can be attributed to the higher water demand of metakaolin and its tendency to promote interparticle flocculation through stronger physicochemical interactions [25] VC^3-1, which had the lowest MK/V ratio, achieved a slump of more than 20 cm, whereas mixtures with higher metakaolin content showed a progressive decrease in fluidity, reaching approximately 18 cm at the highest MK/V ratio.

Fig. 8 and Table 4 present the rheological parameters of the mortar mixtures. For all mixtures, the static yield stress measured at the higher shear rate was approximately 1.5-2 times greater than that obtained at the lower rate, indicating increased flow resistance due to particle rearrangements and strain-dependent effects.

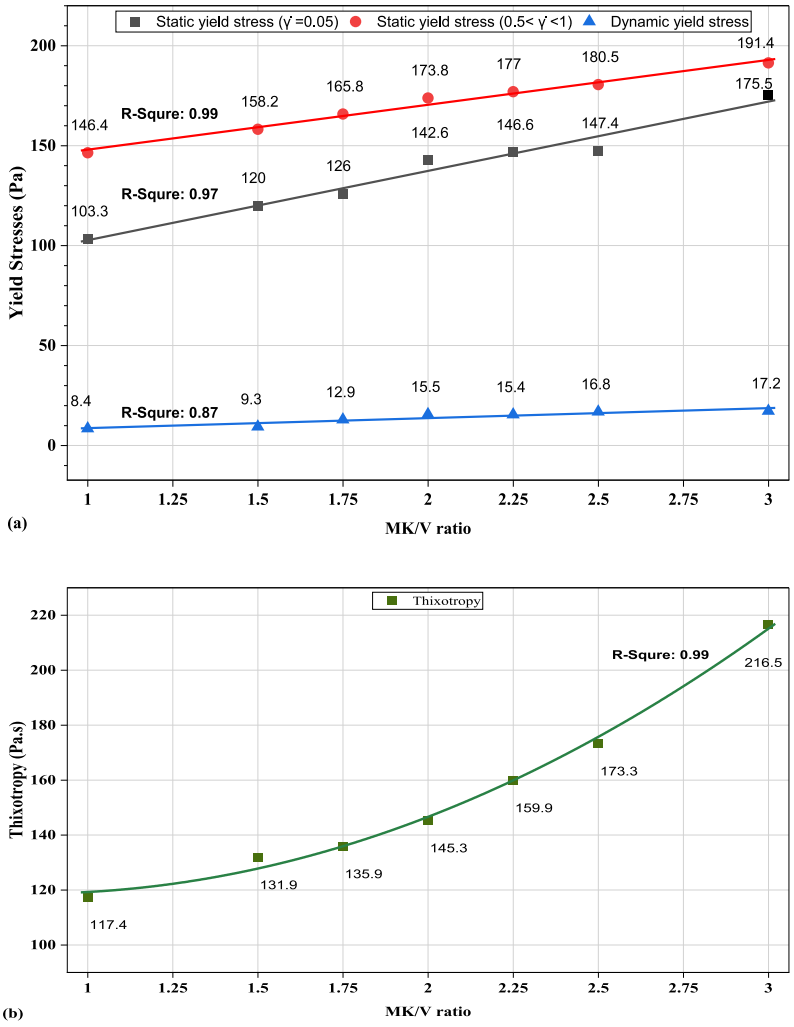

Fig. 8. Rheology specifications of the mortar mixtures, (a) Yield stresses, (b) Thixotropy.

Among the binders, LC^3 exhibited the highest static yield stresses (231.6 Pa at $\dot{\gamma} = 0.05\ s^{-1}$ and 501.7 Pa at $0.5 < \dot{\gamma} < 1\ s^{-1}$). This behavior is attributed to the fine and angular morphology of calcite and metakaolin particles (Figs. 5 and 6), which increases interparticle friction and restricts flowability [46]. In contrast, the VC^3 mixtures, where calcite was replaced with spherical vaterite, displayed substantially lower static yield stresses, reflecting improved flowability due to reduced particle friction.

The raw material particle size distributions (Table 1) exert a profound influence on the packing density and subsequent rheological response of the blended matrices. The synthesized vaterite exhibits a coarser particle size distribution (Dv, 50 = 9.1 μm, Dv, 90 = 17.9 μm) than the calcite (Dv, 50 = 2.9 μm, Dv, 90 = 4.9 μm). Mechanistically, the combination of this coarser profile and the spherical geometry of the vaterite plays a dual role in fluidizing the matrix. First, from a purely geometric standpoint, a sphere possesses the minimum surface-area-to-volume ratio for any given particle size; therefore, the smooth spherical morphology of vaterite inherently yields a lower specific surface area compared to the angular, cubical, or platy geometries of calcite and metakaolin. Consequently, both the larger baseline particle dimension (lower specific surface area) and the morphology of the vaterite particles drastically minimizes the localized water demand required for initial surface wetting, thereby maximizing the volume of "free water" available for hydrodynamic lubrication. Second, these sub-10 μm spheres function via a 'ball-bearing' effect within the suspension, distributed alongside the similarly sized cement grains (Dv, 50 = 11.3 μm). This structural configuration minimizes interparticle friction and mechanical interlocking during shear, effectively lowering the initial yield stress and structural breakdown energy (thixotropy) of the VC^3 systems compared to the fine, angular LC^3 control.

The dynamic yield stress, defined as the minimum stress needed to maintain flow once the material structure has begun to break down, followed a similar trend. LC^3 exhibited the highest dynamic yield stress (40.6 Pa), whereas the VC^3 mixtures showed lower values that gradually increased from 8.4 Pa to 17.2 Pa as the MK/V ratio increased from 1 to 3.

Thixotropy, reflecting the ability of the paste to rebuild its structure at rest and break down under shear, was also highest for LC^3 (352.4 Pa s). The VC^3 mixtures presented moderate thixotropy values, rising from 117.4 Pa s to 216.6 Pa s with increasing MK/V ratio. Mechanistically, the spherical geometry of the synthesized vaterite optimizes the suspension's packing density and significantly moderates the local interstitial void volume between solid phases [47]. Within the VC^3 series, the static yield stress increased linearly while the thixotropy increased nonlinearly with the MK/V ratio, showing a pronounced rise at the highest metakaolin contents. This suggests the presence of threshold effects related to particle packing or structural network formation. This progressive increase in structural breakdown energy is directly linked to the surface chemistry and the higher specific surface area of the calcite and MK compare to vaterite, According to the framework established by Zhao et al. [47] lower specific surface area decreases the probability of direct particle-particle interactions; in this system, the morphology and particle size distribution of the synthesized vaterite yield a lower effective specific surface area, thereby minimizing these physical collisions and lowering initial thixotropy. Overall, these values suggest a balanced rheological profile, combining good flowability with sufficient structural stability, which is desirable for applications such as pumping and 3D printing. Nevertheless, a deeper micro-rheological characterization mapping the exact evolution of zeta potential, water film thickness (WFT), and localized interparticle forces remains an essential next step for future research to provide even more granular insights into the colloidal chemistry of these novel vaterite-bearing matrices.

Overall, while LC^3 binders exhibit workability challenges due to high yield stresses and thixotropy, the VC^3 mixtures offer a promising alternative. The incorporation of spherical vaterite particles reduces both static and dynamic yield stresses and moderates thixotropy, thereby enhancing fresh-state rheology without compromising stability and shape retention. The nonlinear increase in thixotropy with higher MK/V ratios further highlights the complex microstructural interactions at play and underscores the need for careful optimization of the mix design.

3.2. Setting time and isothermal calorimetry analysis

The results in Table 5 show that the blended mixtures exhibited setting times ranging from 91 to 125 min. Replacing calcite with vaterite resulted in an increase in setting time, rising from 91 min (LC^3) to 119 min for mixtures with the same metakaolin-to- carbonate ratio (VC^3-2). Within the VC^3 series, increasing the metakaolin content led to an overall reduction in setting time, although some fluctuations were observed. To gain deeper insight into the hydration behavior, isothermal calorimetry tests were performed in quadruplicate, allowing a more precise evaluation of hydration kinetics and setting characteristics.

Fig. 9 and Table S1 present the estimated setting behavior derived from the heat evolution profiles. Consistent with the setting-time

Table 4
Rheological parameters of the mortar mixtures.

Name	Static yield stress (Pa)		Dynamic yield stress (Pa)	Thixotropy (Pa.s)
	($\dot{\gamma} = 0.05$)	($0.5 < \dot{\gamma} < 1$)		
LC^3	231.5	501.6	40.5	352.4
VC^3-1	103.3	146.4	8.4	117.4
VC^3-1.5	120.0	158.2	9.3	131.9
VC^3-1.75	126.0	165.8	12.9	135.9
VC^3-2	142.6	173.8	15.5	145.3
VC^3-2.25	146.6	177.0	15.4	159.9
VC^3-2.5	147.4	180.5	16.8	173.3
VC^3-3	175.5	191.4	17.2	216.5

Table 5
Setting time of mortar mixtures according to UNE-EN 1015-9.

Mixture	LC^3	VC^3 1	VC^3 1.5	VC^3 1.75	VC^3 2	VC^3 2.25	VC^3 2.5	VC^3 3
Setting time (min)	91	125	116	123	119	105	100	100

measurements, the isothermal calorimetry results indicate that VC^3 mixtures generally exhibited longer setting times than LC^3. To compare the hydration kinetics among the VC^3 binders, three key parameters were evaluated: (a) time of the maximum dQ/dt (d^2Q/dt^2 equals to zero), the turning point of the main curve as initial setting time (IST) [48], (b) the time of the main peak when the dQ/dt equals to zero as final setting time (FST) [48], and (c) the time corresponding to 50% of the main-peak heat release [49].

The time of the turning point of the main curve decreased progressively as the MK/V ratio increased, from approximately 120 min, at a ratio MK/V of 1, to about 108 min at the highest MK/V ratios. This trend reflects a faster transition from the dormant (induction) phase to the acceleration phase with increasing metakaolin content (Fig. 9a–I). Similarly, the time at 50% of the alite-peak heat also decreased, from ~190 min at MK/V = 1 to ~180 min at the highest ratio. This parameter was determined according to ASTM C1679 [49], which correlates the time to 50% of the main hydration peak with initial setting. The main (alite)-peak time showed a comparable, though modest, shift of approximately 10 min across the series, further supporting the observation that higher metakaolin

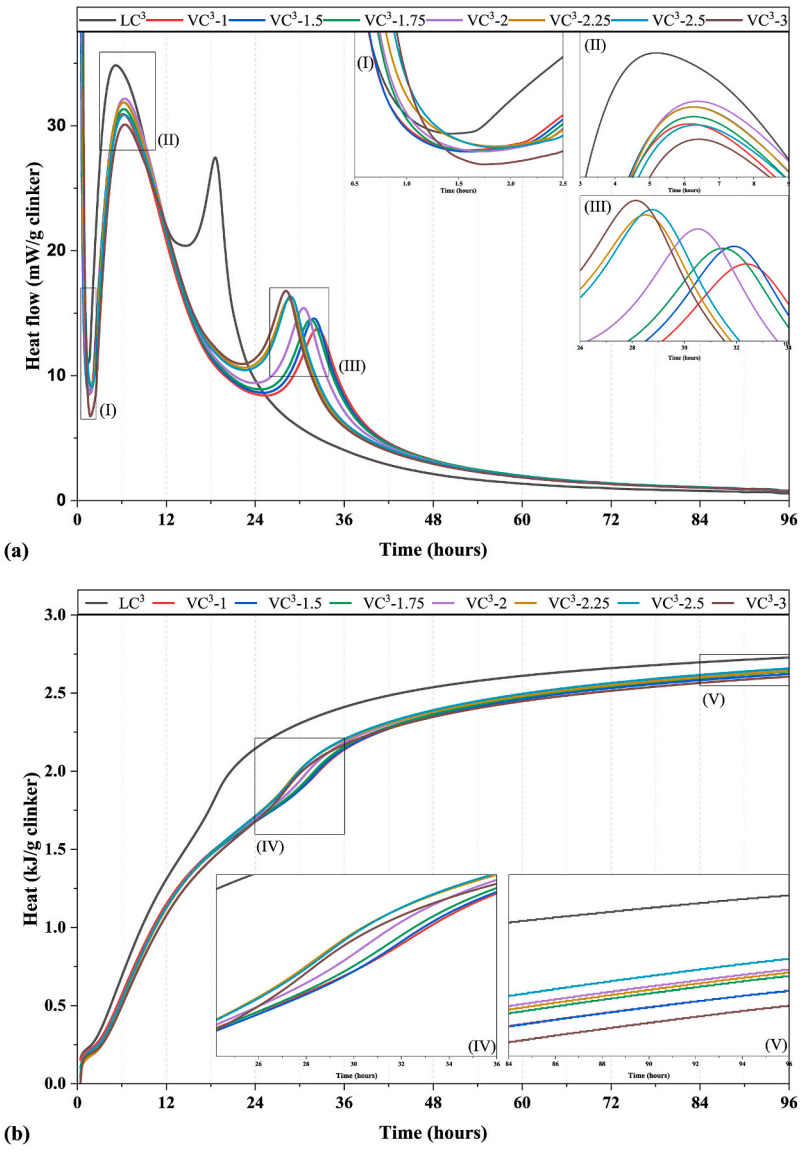

Fig. 9. Isothermal calorimetry results of paste mixtures: (a) heat flow of hydration and (b) cumulative heat released during hydration.

content accelerates early hydration (Fig. 9a–II).

The aluminate (second) peak (Fig. 9a–III) displayed distinct behavior. In LC^3, it occurred much earlier (around 10 h) and covered a narrower duration, indicating a faster and more concentrated aluminate reaction as reported in a previous study [34]. Fig. 9a indicates that, for the VC^3 mixtures, both the second peak duration and integral decreased with increasing MK/V ratio: the duration shortened from approximately 22 h to 16 h, and the total released heat declined from ~170 J/g to ~160 J/g, with minor fluctuations (Fig. 9a–IV and 9a-V). Conversely, peak amplitude increased progressively (from 7.2 mW/g in VC^3-1 to 8.4 mW/g in VC^3-3), suggesting that higher metakaolin content intensified the aluminate reaction despite the shorter reaction window. This performance can be probably ascribed to the fact that MK acts as a source of Al, in line with its chemical and mineralogical composition (see section 2.1).

In addition, these systematic shifts in hydration parameters can be attributed to a surface-mediated mechanism arising from the reported ability of vaterite to adsorb calcium and sulfate ions [50]. At lower MK/V ratios, the higher vaterite content exhibits strong affinity for Ca^{2+} and SO_4^{2-} ions, limiting their early availability and thereby delaying both aluminate and silicate hydration reactions, as demonstrated in our earlier study [34]. This "ion-sink" effect extends the induction period and postpones the main hydration peak (Fig. 9a–II). As the proportion of vaterite decreases, the sequestration effect weakens, increasing the ability of free Ca^{2+} and sulfate for early hydration. Additionally, the finer particle size and higher surface area of metakaolin promote greater reactivity. As a result, the induction and alite peaks shift earlier, and the aluminate peak becomes sharper and more pronounced.

The relatively small magnitude of these temporal shifts suggests that although ionic availability improves at higher MK/V ratios, this effect is partially offset by the reduced number of carbonate-based nucleation sites. This interaction yields a balanced overall hydration response across the VC^3 series.

3.3. Compressive strength

Fig. 10 shows the compressive strength development of LC^3 and VC^3 mortars at 3, 7, 28, and 91 days. At 3 days, VC^3-1 exhibited slightly higher strength than LC^3 (ca. 14.7 MPa vs. 13.8 MPa), corresponding to a 107% of LC^3. Most of the other VC^3 mixtures showed reduced early-age performance, with strengths ranging between 84% and 101% of LC^3. The lowest value was recorded for VC^3-3 (ca. 11.5 MPa), representing an 84% of LC^3. This early-age reduction strength is attributed to the slower dissolution kinetics of vaterite, as reported previously [34].

By 7 days, the effect of binder composition became more pronounced. VC^3-1 and VC^3-1.5 remained similar to LC^3 (ca. 14-15 MPa, 95-96% of LC^3), while mixtures with higher MK/V ratios showed substantial strength gains. VC^3-2 reached ca.17.7 MPa (116% of LC^3),

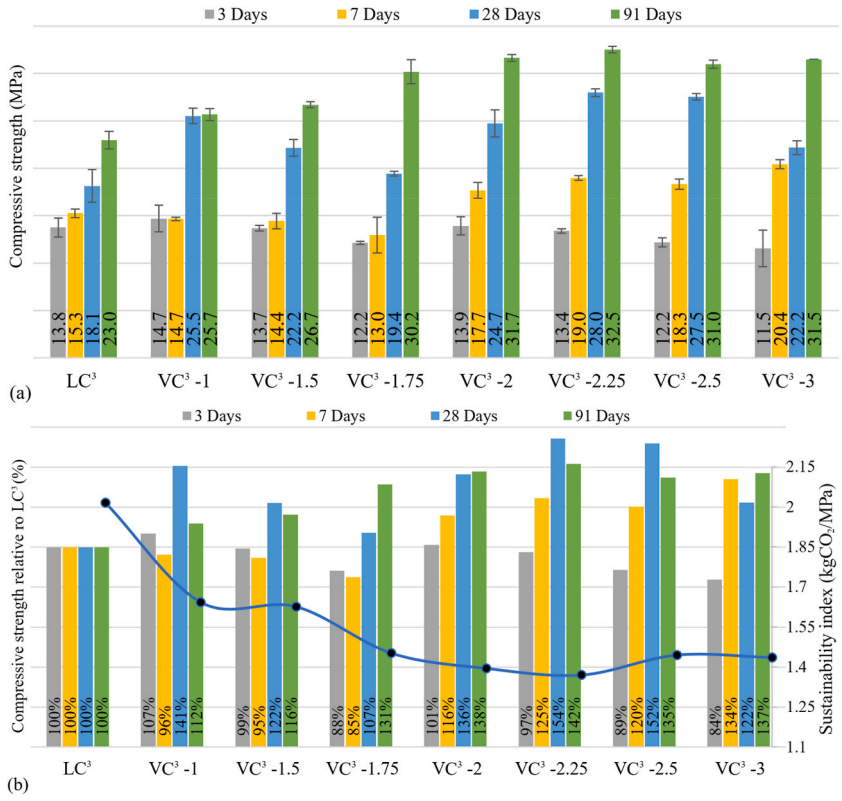

Fig. 10. Compressive strength of the composites at different curing ages: (a) absolute compressive strength and (b) sustainability index at 91 days, together with compressive strength values normalized to the LC^3 mixture.

and VC^3-3 achieved ca. 20.4 MPa (134% of LC^3). These results indicate that the vaterite begins to exert a greater contribution beyond very early ages.

At 28 days, the beneficial effect of incorporating vaterite became clearer. Most VC^3 mortars surpassed LC^3 (18.1 MPa), with VC^3-2.25 and VC^3-2.5 reaching approximately 28 MPa (154% and 152% of LC^3, respectively). Even mixtures with intermediate MK/V ratios, such as VC^3-1.5 and VC^3-1.75, attained 22-23 MPa (122-107% of LC^3), confirming that vaterite contributes to sustained hydration once its slower initial dissolution is overcome.

By 91 days, all VC^3 mortars outperformed LC^3 (23.0 MPa). Strengths ranged from 26.7 MPa (VC^3-1.5, 116% of LC^3) to more than 32 MPa for VC^3-2.25 (142% of LC^3). The relationship with MK/V ratio was nonlinear: strength increased steadily between MK/V ratios of 1.0 and 2.5, then declined at MK/V = 3. This suggests that, although metakaolin provides reactive alumina to sustain hydration, excessive MK at the expense of vaterite disrupts the optimal balance required for maximizing long-term performance. Further details are explained in section 3.5 (Thermogravimetric analysis).

In summary, VC^3 mortars displayed reduced strength at very early ages due to the limited initial reactivity of vaterite, but strength development accelerated markedly from 7 days onward. The optimal MK/V range of 2.0-2.5 delivered the highest 28- and 91-day strengths, highlighting the complementary roles of metakaolin and vaterite in balancing early formation of hydration products with long-term mechanical development. These mechanical trends align with and are further supported by the TGA and XRD analyses discussed in the subsequent sections.

3.4. Sustainability indicator

The quantitative evaluation of the Si in Fig. 10b shows that the VC^3 system significantly outperforms both the LC^3 reference. Si index is generally lower in calcined clay cements, and this performance is initially rooted in the substantial replacement of Portland clinker with metakaolin, a fundamental mechanism that reduces the CO_2 footprint across all ternary binders [21]. While, the VC^3 system achieves a superior 31.6% improvement in sustainability efficiency over LC^3 due to two additional factors: the incorporation of vaterite provides a distinct advantage because its negative CO_2 footprint that achieved through synthesis via carbon capture and mineralization; and second, the synergistic integration between the calcined clay and vaterite that maximize compressive strength, further lowering the S_i by delivering higher mechanical performance per unit of carbon emitted.

3.5. Thermogravimetric analysis

Thermogravimetric analysis was conducted to assess the progression of hydration and carbonation reactions in LC^3 and VC^3 mortars (Fig. 11 and Table 6). Interpretation focused on three primary temperature intervals: 105-350 °C, corresponding to the release of bound water from C-(A)-S-H and AFt/AFm phases; 420-480 °C, representing the dihydroxylation of portlandite (CH); and 600-800 °C, associated with the decarbonation of calcium carbonates such as calcite and vaterite.

While isothermal calorimetry successfully captures the initial hydration kinetics and early ionic reactivity thresholds of the binders,

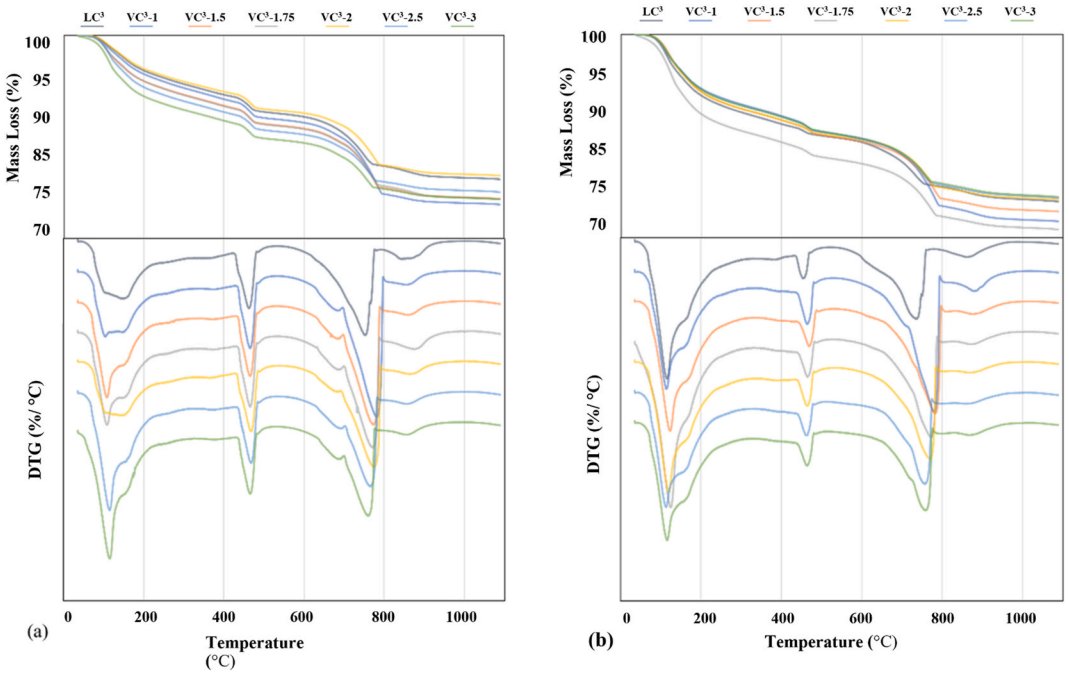

Fig. 11. Thermogravimetric (TG) and differential thermogravimetric (DTG) curves of the samples: (a) at 7 days and (b) at 91 days.

the highly compressed cumulative heat curves at 3 days make it challenging to isolate the discrete physical-chemical drivers responsible for early mechanical variations. To resolve this limitation and establish a direct quantitative link, the 3-day compressive strength development can be correlated with the corresponding TGA mass loss intervals of the mortar specimens. At 3 days, macro-mechanical performance is fundamentally governed by the absolute volume of early space-filling hydration products accumulated within the matrix, rather than the global thermal energy baseline. The peak early-age strength observed for VC^3-1 (14.7 MPa) tracks consistently with its maximum chemically bound water mass loss of 6.8% in the 105–350 °C thermal window, which directly signifies an enriched initial precipitation of main hydration products such as ettringite and early-stage C-(A)-S-H gels. As the metakaolin content increases, the reduction in 3-day compressive strength down to its minimum value in VC^3-3 (11.5 MPa) is precisely mirrored by a localized contraction in bound water content down to 6.3%. Concurrently, the TGA mass loss in the 420–480 °C region displays a progressive decrease from 2.19% (VC^3-1) down to 2.07% (VC^3-3). While portlandite is a primary product of cement clinker hydration, this narrow variation confirms that meaningful pozzolanic consumption of calcium hydroxide has not yet extensively occurred at 3 days. Consequently, because the pozzolanic turnover has not yet matured into highly interconnected, rigid amorphous aluminosilicate gel networks at this early stage, the 3-day mechanical performance remains explicitly synchronized with the absolute quantity of early hydrates captured in the bound water domain.

At 7 days, the bound-water mass loss in the 105-350 °C range increased from 7.2% (VC^3-1) to 8.7% (VC^3-3), indicating that higher MK/V ratios promote greater hydrate formation. This trend closely reflects the 7-day compressive strength data reported in Section 3.3, where strength increased from 14.7 MPa to 20.4 MPa across the same mixtures. These results show that mortars containing more metakaolin produce a higher volume of hydration products during early curing, whereas vaterite-rich mixtures hydrate more slowly. The LC^3 reference mixture showed a significantly lower bound-water content (6.8%), consistent with its more limited early-age reactivity and corresponding strength of approximately 15.3 MPa.

The mass loss associated with portlandite dihydroxylation (420-480 °C) decreased slightly from 2.28% (VC^3-1) to 2.12% (VC^3-3), suggesting enhanced pozzolanic consumption of CH and the formation of additional secondary hydrates. Because the VC^3 mixtures contain different initial amounts of vaterite, the mass loss in the 600–800 °C interval was normalized to the vaterite content specified in the mix design (Fig. 12). Normalization allows direct comparison of carbonate reactivity across mixtures. While the absolute carbonate mass loss decreased from 10.53% (VC^3-1) to 6.78% (VC^3-3), the normalized ratio of mass loss to initial vaterite content increased from 0.47 to approximately 0.61. This indicates that, at higher MK/V ratios, a smaller proportion of vaterite participates in hydration reactions. The results suggest that increased metakaolin content reduces the involvement of vaterite in early hydration and favors the formation of C-(A)-S-H phases. Thus, the decrease in absolute carbonate-related mass loss does not reflect more extensive carbonate consumption; rather, it indicates less efficient utilization of vaterite when metakaolin is more abundant.

At 91 days, the bound-water content continued to increase across the VC^3 mixtures, rising from approximately 9.2% (VC^3-1) to a maximum of about 11.1%, and then decreasing to around 9.4% (VC^3-3). This behavior mirrors the long-term compressive strength trends described in Section 3.3, where strength increased from 25.7 MPa (VC^3-1) to over 32 MPa (VC^3-2.25), followed by a slight decline at the highest MK/V ratios. The close correspondence between bound-water content and mechanical performance confirms that long-term strength development is governed by continued formation of hydration products, particularly in mixtures with intermediate MK/V ratios.

The CH-related mass loss at 91 days declined from 1.75% (VC^3-1) to 1.47% (VC^3-2), followed by a slight increase to about 1.54% in mixtures with higher MK/V ratios. The consistently low CH mass loss throughout the series suggests that most portlandite produced during cement hydration was consumed through ongoing pozzolanic reactions and carboaluminate formation.

Overall, the TGA results demonstrate a strong relationship between thermal behavior and mechanical performance. Higher MK/V ratios enhance hydrate formation and improve strength development up to an optimal range; however, excessive metakaolin reduces the participation of vaterite in hydration and slightly diminishes long-term performance. These findings highlight the complementary roles of metakaolin and vaterite in governing hydration kinetics, microstructural evolution, and mechanical properties.

3.6. XRD quantitative phase analysis

At 7 days, the quantitative XRD results (Fig. S1 and Fig. 13) provide direct evidence of the microstructural and mineralogical transformations inferred from the TGA and compressive strength data. The amorphous phase content, primarily representing C-(A)-S-H gel and poorly crystalline hydrates [51,52], increased from approximately 40 g/100g_{binder} in the mixtures with low MK/V ratios

Table 6
Thermogravimetric (TG) mass loss of the samples at 7 and 91 days.

	Temperature range (°C)	LC^3	VC^3-1	VC^3-1.5	VC^3-1.75	VC^3-2	VC^3-2.25	VC^3-2.5	VC^3-3
3 Days	105-350	6.6	6.8	6.5	6.4	6.4	6.3	6.4	6.3
	420-480	2.11	2.19	2.12	2.10	2.10	2.09	2.10	2.07
	600-800	7.0	10.5	8.2	8.3	7.6	7.5	7.2	7.1
7 Days	105-350	6.8	7.2	7.6	7.8	6.5	7.6	8.5	8.7
	420-480	2.1	2.3	2.2	2.2	2.1	2.2	2.2	2.1
	600-800	7.3	10.5	8.8	8.4	7.7	7.5	7.0	6.8
91 Days	105-350	10.1	9.2	10.1	11.4	10.0	11.1	9.4	9.4
	420-480	1.2	1.8	1.6	1.6	1.5	1.3	1.5	1.5
	600-800	6.6	10.0	8.4	7.8	7.1	7.9	6.7	6.6

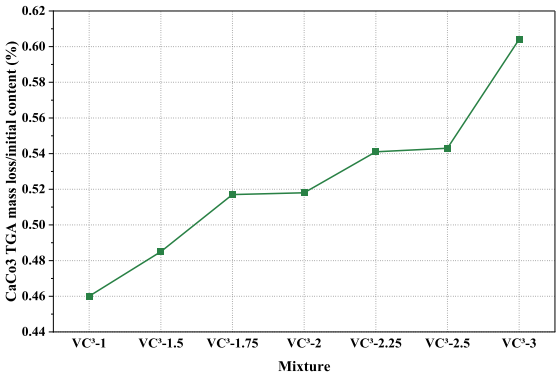

Fig. 12. Calcium carbonate ($CaCO_3$) mass loss at 7 days, normalized to the initial vaterite content.

(VC^3-1 and VC^3-1.5) to about 46 g/100g_{binder} in the mixtures with higher MK/V ratios (VC^3-2.5 and VC^3-3), with a small fluctuation at intermediate values. This progressive increase aligns well with the rise in bound water measured in the 105-350 °C interval by TGA (from 9.4 to 11.5 g/100g_{binder}) and with the corresponding improvement in compressive strength (from 14.7 MPa to 20.4 MPa). These results confirm that higher MK/V ratios promote the formation of a larger volume of hydration products at the early stage.

Fig. 13 indicates that, among the crystalline hydrates, ettringite increased from 7.3 g/100g_{binder} (VC^3-1) to 9.9 g/100g_{binder} at the highest MK/V ratio (with a maximum for the VC^3-2.25 sample), indicating intensified aluminate-sulfate reactions driven by metakaolin. Monocarboaluminate, known to densify the microstructure [53], was detected in all mixtures, ranging from 1.1 g/100g_{binder} (VC^3-1) to 2.1 g/100g_{binder} (VC^3-3), demonstrating that even a portion of the available carbonate participates in AFm formation even at an early age. These observations are consistent with the TGA results, which showed increasing bound water contents and slightly decreasing portlandite fractions, reflecting active pozzolanic and carboaluminate reactions that correspond to higher compressive strengths.

At 91 days, the XRD plot (Fig. S1) shows that hydration has progressed further, producing a more mature and chemically stable phase assemblage. These changes are fully consistent with the long-term TGA and compressive strength trends, both of which show peak performance around MK/V ratios of approximately 2.0-2.25. The amorphous content remained high across all VC^3 mixtures, ranging from 42.5 g/100g_{binder} (VC^3-1) to 46.83 g/100g_{binder} (VC^3-2.5), followed by a slight decline to 42.8 g/100g_{binder} (VC^3-3). This represents a clear increase relative to the 7-day values and confirms ongoing formation of secondary C-(A)-S-H and AFm hydrates beyond early curing. Mixtures with intermediate MK/V ratios (1.75-2.5) exhibited the highest amorphous contents, corresponding to the maximum bound-water value (~11.5%) and the highest 91-day compressive strengths (>32 MPa for VC^3-2.25).

Monocarboaluminate contents increased slightly at 91 days, reaching 0.8-2.8 g/100g_{binder}, reflecting sustained interactions between carbonate and aluminate phases (Fig. 13). Minor crystalline phases such as tobermorite-like C-S-H (0.74-1.3 g/100g_{binder}) and mullite (2.7-5.4 g/100g_{binder}) remained stable, indicating that most structural development occurred within the amorphous and AFm domains rather than through major changes in crystalline hydrates.

Portlandite contents measured by XRD remained low, with the lowest value observed for VC^3-2.5 (1.7 g/100g_{binder}). This reduction corresponds to the compositions with the highest mechanical strength and is consistent with TGA measurements in the 420-480 °C interval. These results confirm that portlandite continued to be consumed through pozzolanic and carboaluminate reactions throughout curing. The retention of low percentages of CH at 91 days suggests that the system was approaching equilibrium between clinker hydration and CH consumption. This explains the continued increase in amorphous content and bound water, reflecting the sustained incorporation of calcium into stable C-(A)-S-H and AFm phases and the densification of the hardened matrix.

The persistently low calcite levels indicate that most vaterite was either dissolved or transformed into carboaluminate phases rather than recrystallizing. The increase in monocarboaluminate content up to 2.8 g/100g_{binder} supports these conclusions. Collectively, these results demonstrate a gradual shift from metastable vaterite toward chemically bound carbonate-aluminate phases, consistent with the observed increases in amorphous hydrates and long-term mechanical performance.

To systematically consolidate the quantitative link between long-term phase evolution and mechanical performance, the nonlinear compressive strength drop observed at the highest metakaolin content (VC^3-3) can be interpreted through a space-filling structural model driven by stoichiometric balance. At 91 days, long-term engineering performance is strictly regulated by maintaining an optimized chemical equilibrium between the reactive aluminosilicate content and the available carbonate reservoir. In the optimal range (MK/V = 2.0–2.5), the balanced dissolution-precipitation loop maximizes the space-filling hydrate network, driving the amorphous phase content to its peak at 46.83 g/100g_{binder} (VC^3-2.5), minimizing residual portlandite to 1.7 g/100g_{binder}, and sustaining the maximum compressive strengths exceeding 32 MPa. Conversely, elevating the MK/V ratio to 3.0 (VC^3-3) induces a clear carbonate limitation phenomenon. Despite an abundance of reactive alumina, reducing the initial vaterite content to 11.2 g/100g_{binder} limits the system's capacity to continuously precipitate space-filling carboaluminate phases. This stoichiometric restriction is quantitatively validated by the synchronized contraction of the total 91-day amorphous phase back to 42.8 g/100g_{binder} and the lower TGA bound water content of 9.4%. This multi-analytical correlation demonstrates that long-term strength development is not a simple linear function of pozzolanic substitution, but relies on a precise mineralogical balance necessary to optimize matrix refinement.

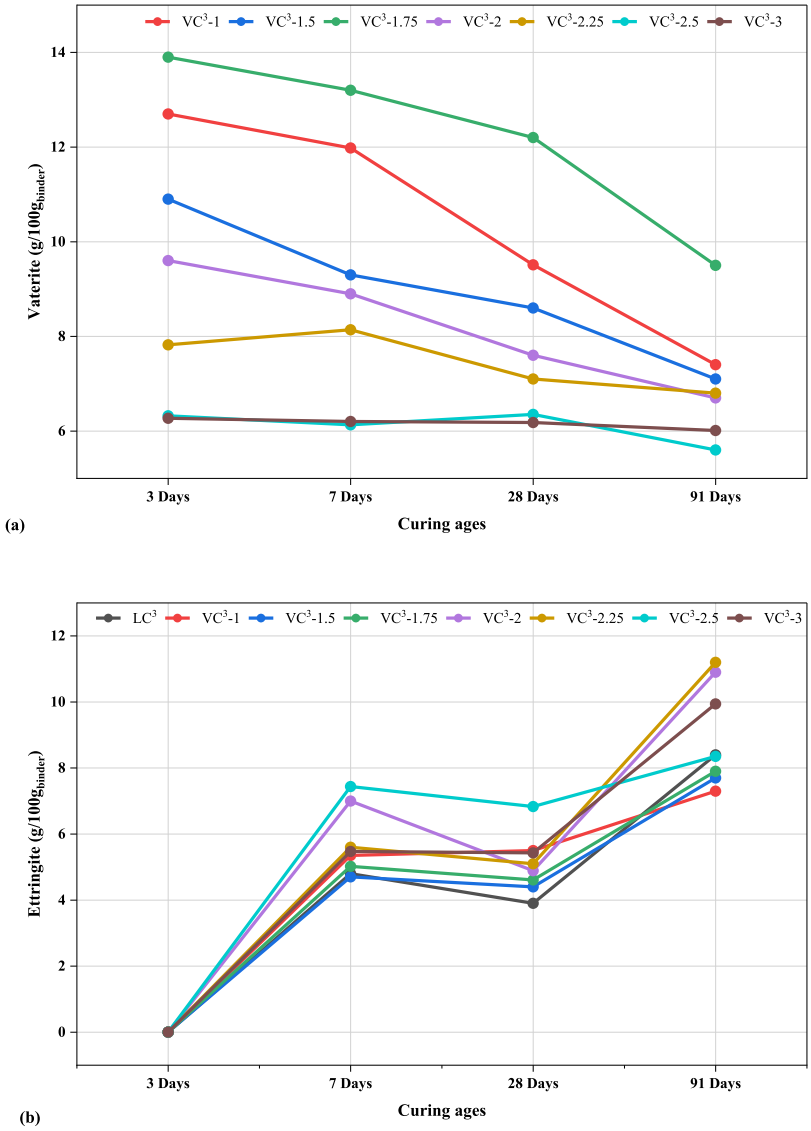

Fig. 13. XRD quantitative phase analysis of the samples at 3, 7, 28, and 91 days of curing: (a) Calcium Carbonates (Vaterite), (b) Ettringite, (c) Monocarboaluminates, and (d) Portlandite.

3.7. SEM analysis

At 3 days, the microstructure of the VC^3 mortars reveals clear differences between the mixtures with the lowest and highest MK/V ratios, consistent with their early-age mechanical performance. In VC^3-1, numerous needle-like ettringite crystals are observed filling pores and growing on the surfaces of vaterite grains (arrows in Fig. 14a). This confirms that the fine carbonate particles act as effective nucleation sites, promoting early hydration. In contrast, VC^3-3 exhibits fewer and shorter ettringite needles (arrows in Fig. 14b), reflecting its reduced calcium carbonate content and increased metakaolin proportion. The diminished ettringite formation corresponds well with the slightly delayed early strength development of VC^3-3 and confirms that calcium carbonate enhances early hydration primarily through physical seeding rather than chemical reaction.

At 7 days, the differences between the mixtures become more pronounced, marking the shift from initial hydration to secondary pozzolanic and carbonate-aluminate reactions. In VC^3-1 (Fig. 14c), large, tabular portlandite crystals remain embedded in a relatively open matrix with limited formation of gel products, indicating that much of the vaterite remains largely unreacted at this stage. Since the morphology and crystal size of portlandite can vary significantly based on microstructural constraints [54,55], the specific phase

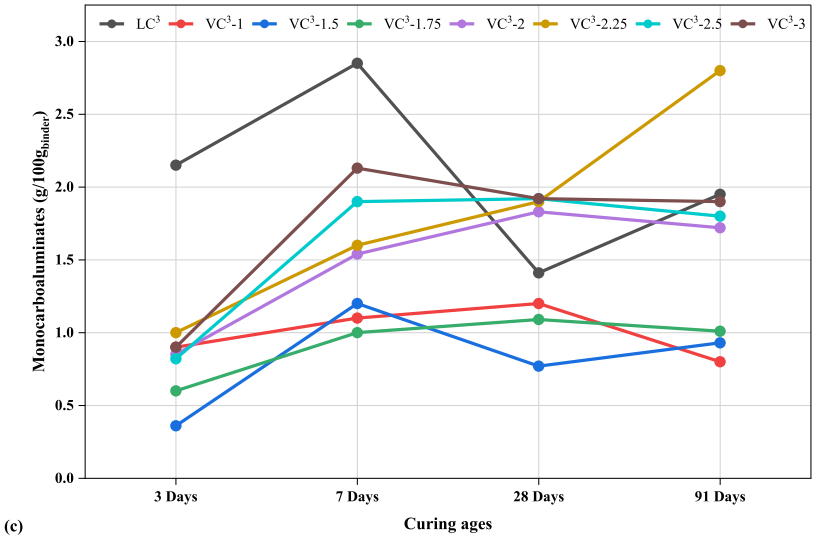

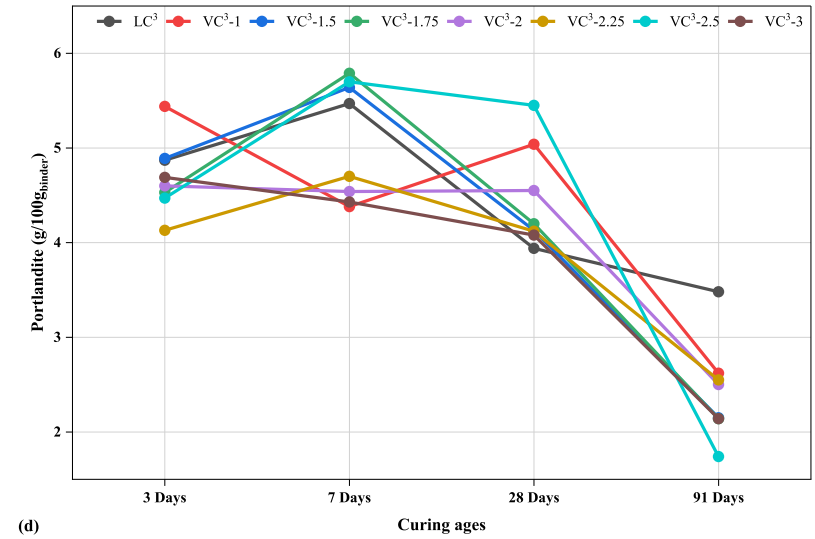

Fig. 13. (*continued*).

assignment here was definitively verified through localized EDS elemental mapping. In VC^3-3 (Fig. 14d), the microstructure is considerably denser, with partially dissolved metakaolin particles surrounded by fine aluminosilicate gel (arrows in Fig. 14d). The reduced presence of portlandite suggests active pozzolanic consumption. This is quantitatively substantiated by the XRD Rietveld refinement data (Table 5, Fig. 13) and TGA mass loss profiles, which reveal a systematic drop in residual CH content down to just 1.7 g/100g_{binder} for the VC^3-2.5 matrix, directly coinciding with the peak accumulation of the amorphous C-(A)-S-H gel phase.

At 91 days, the divergence between the systems is even more distinct. In VC^3-1 (Fig. 14e), numerous undecomposed vaterite grains persist within a coarse and heterogeneous matrix, indicating limited progression of pozzolanic and carboaluminate reactions and explaining the lower late-age strength of this mixture. In contrast, the VC^3-3 microstructure (Fig. 14f) is compact and homogeneous, dominated by an interlocking matrix of aluminosilicate hydrates, which were chemically verified via localized SEM-EDS mapping showing overlapping Al and Si signals (Fig. S2). Vaterite grains appear roughened and partially dissolved, while portlandite is largely absent, demonstrating the advanced stage of metakaolin-lime-carbonate reactions. The resulting dense matrix demonstrates the long-term reactivity of vaterite and its synergistic interaction with metakaolin, which together refine the pore structure and sustain continued strength development.

Elemental mapping at 91 days (Figs. 15 and 16) shows that the VC^3 binder consists of several coexisting hydrate families rather than a single dominant phase. The continuous matrix surrounding the reacted grains is enriched in Ca with detectable Si, and locally

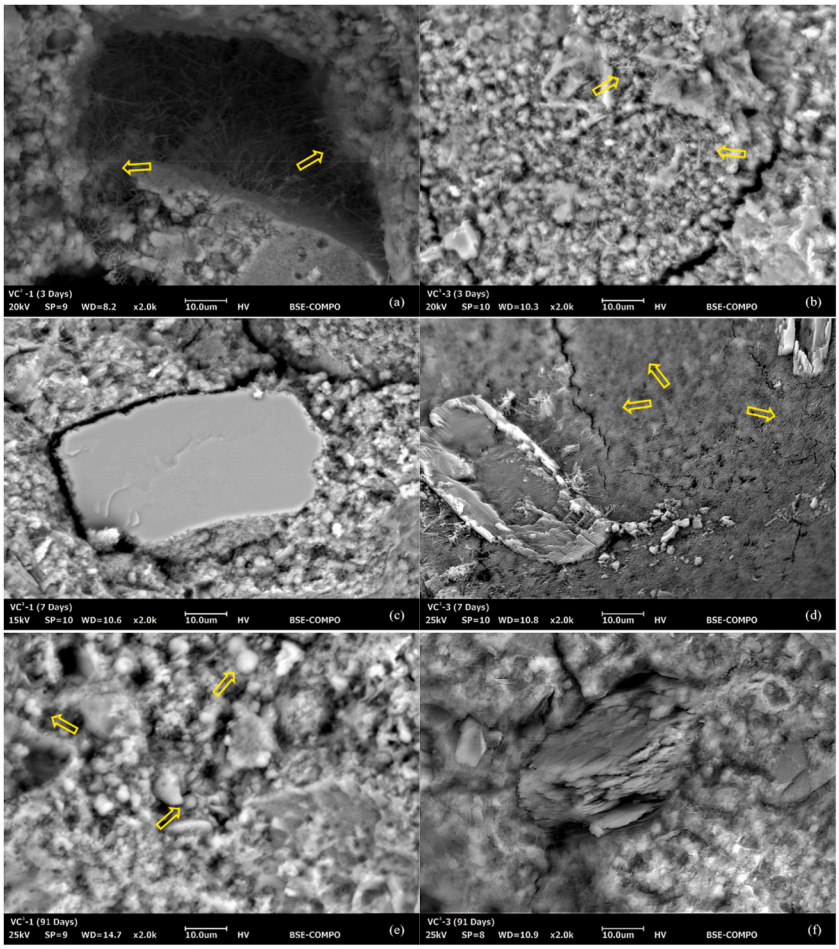

Fig. 14. SEM images showing the microstructural development of VC^3 mortars at different curing ages: (a) VC^3-1 at 3 days, (b) VC^3-3 at 3 days, (c) VC^3-1 at 7 days, (d) VC^3-3 at 7 days, (e) VC^3-1 at 91 days, and (f) VC^3-3 at 91 days.

enriched in both Ca and Al. This composition is consistent with calcium and silicate hydrate (C-S-H/C-A-S-H) together with calcium-aluminate hydrates of the AFm family. In certain regions, these Ca-Al-rich domains contain very little Si, indicating the formation of carboaluminate-type AFm phases associated with the carbonate-rich system. In parallel, large zones, extending over several hundred micrometers, display strong enrichment in Al and Si, along with localized Na- and K-rich areas, while remaining Ca-poor. These

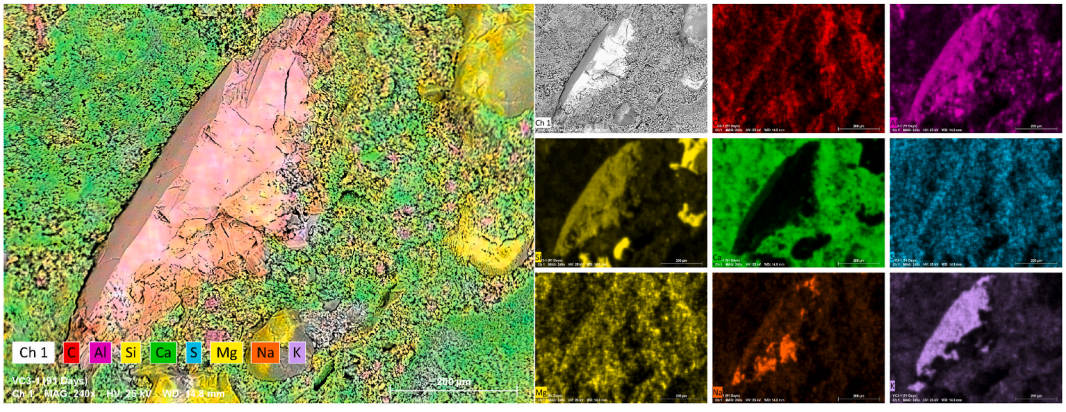

Fig. 15. SEM image (240x) of the VC^3-1 mortar at 91 days, accompanied by EDS elemental mapping showing the spatial distributions of carbon (C), aluminum (Al), silicon (Si), calcium (Ca), sulfur (S), magnesium (Mg), sodium (Na), and potassium (K).

features are characteristic of aluminosilicate hydrates derived from metakaolin, forming Na/K-A-S-H-type gels. The coexistence of Ca-Si hydrates, Ca-Al carboaluminate phases, and aluminosilicate gels demonstrates that, by 91 days, the VC^3 matrix has developed into a chemically complex and spatially continuous multiphase binder. This assemblage fills the microstructure, forms a dense interfacial zone around sand particles, and accounts for the refined pore structure and high compressive strength observed at later ages.

Higher-magnification imaging (2000×) confirms that this chemical assemblage is uniformly developed throughout the VC^3 matrix. At this scale, the binder consists of intermixed calcium silicate hydrates (C-S-H/C-A-S-H), aluminosilicate gels, and localized calcium-aluminate phases, while occasional sulfate-enriched spots indicate residual ettringite. These hydrates form a dense and continuous network that extends into the interfacial transition zone, where the C-S-H-rich matrix tightly adheres to the quartz sand particles, producing a compact and well-integrated ITZ. The coexistence of these hydrates at both macro- and micro-scales highlights the chemically diverse and interconnected nature of the VC^3 binder, which underpins its refined microstructure and high late-age compressive strength.

4. Conclusions

This study systematically evaluated the influence of the metakaolin-to-vaterite (MK/V) ratio on the fresh, mechanical, and microstructural performance of vaterite-calcined clay (VC^3) mortars, using limestone-calcined clay (LC^3) as a reference system. The findings demonstrate that adjusting the binder composition fundamentally affects hydration kinetics, phase assemblage, and microstructural development, and metakaolin acts as the primary chemical driver. These compositional effects, according to the active pozzolanic nature of the calcined clay, govern the balance between early-age reactivity, long-term strength, and rheological behavior, providing a deeper understanding of how vaterite interacts synergistically with calcined clay in low-clinker ternary systems. The fresh-state performance of VC^3 mortars was strongly governed by the interplay between metakaolin and vaterite. Replacing calcite with vaterite improved flowability and reduced the static and dynamic yield stress due to the spherical morphology of vaterite. However, increasing the MK/V ratio led to higher yield stress and thixotropy. This suggests that the calcined clay content should be precisely tuned to provide a rheological profile. Despite this, the VC^3 mixtures maintained a favorable rheological profile that combined workable flow with adequate structural stability, making them more suitable than LC^3 for applications such as pumping, extrusion, and potentially 3D printing.

Setting time and early hydration kinetics were influenced by the MK/V ratio. The substitution of calcite with vaterite generally increased the setting time compared with LC^3. Within the VC^3 series, early hydration behavior was controlled by competing mechanisms: vaterite's high surface-related adsorption capacity for Ca^{2+} and SO_4^{2-} ions tended to temporarily delay initial hydration by altering early pore solution concentrations—a surface-affinity mechanism explicitly validated via electrokinetic and zeta potential evaluations in our previous work [50]. While the pozzolanic reactivity of metakaolin promoted faster progression of the hydration process. As a result, mixtures with higher MK/V ratios showed slightly accelerated hydration relative to vaterite-rich binders.

In terms of mechanical performance, VC^3 mortars exhibited slightly lower early-age compressive strength than LC^3, although the mixture with the lowest MK/V ratio performed marginally better at 3 days. After 7 days, this trend reversed, and all VC^3 mixtures exceeded the strength of LC^3. Strength increased steadily with the MK/V ratio up to approximately 2.0-2.5, where the highest 28- and 91-day strengths were achieved, reaching values up to 42% greater than those of LC^3. This improvement reflects the complementary roles of vaterite and metakaolin: the reactive carbonate content of vaterite and the pozzolanic activity of metakaolin together promote the formation of additional hydrate phases and the development of a denser, more cohesive matrix.

From a sustainability perspective, although ternary binders inherently possess a lower CO_2 footprint due to the substantial replacement of Portland clinker with calcined clays, vaterite offers important advantages, as it can be synthesized through CO_2 capture and mineralization, making it a carbon-negative carbonate source. The calculated sustainability index confirmed that VC^3 binders were environmentally more efficient than LC^3, demonstrating their potential as a viable pathway toward low-clinker and reduced-

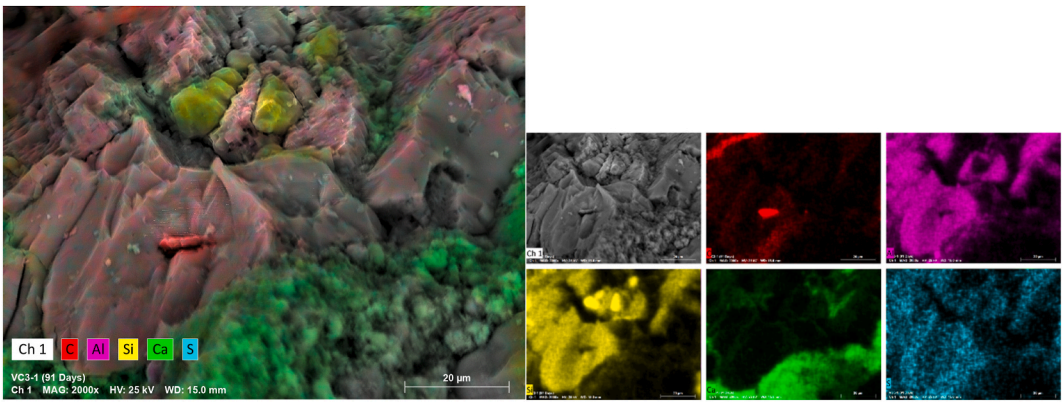

Fig. 16. SEM image (2000x) of the VC^3-1 mortar at 91 days, with corresponding EDS elemental mapping of carbon (C), aluminum (Al), silicon (Si), calcium (Ca), and sulfur (S).

carbon cementitious technologies.

The phase assemblage results further support the synergistic interaction between metakaolin and vaterite. The amorphous content increased from approximately 40 g/100g_{binder} at 7 days to nearly 46 g/100g_{binder} at 91 days, mirroring the growth in bound water and strength. The low portlandite contents and the formation of monocarboaluminate confirmed that both pozzolanic and carbonate–aluminate reactions were active and continued throughout curing.

Microstructural analysis revealed that the VC^3 mixtures facilitated the formation of a multiphase matrix composed of monocarboaluminate and highly cross-linked C-(A)-S-H gels. This chemically complex assemblage refined the pore structure, contributed directly to the superior long-term mechanical performance observed in mixtures with intermediate MK/V ratios. SEM and EDS analyses showed a clear transition from heterogeneous, vaterite-rich matrices at an early age to dense networks of C-S-H, C-A-S-H, and aluminosilicate gels at 91 days. The hydrates formed a compact interfacial transition zone around the sand grains, explaining the marked strength gain at later ages.

Overall, while metakaolin functions as the reactive aluminosilicate backbone in ternary binding systems, vaterite functions not only as a reactive carbonate phase but also as a key component that enhances rheology, supports sustained hydration, and drives microstructural refinement. The combined technical and environmental benefits highlight VC^3 as a promising next-generation binder system for sustainable cementitious materials.

Future research should focus on evaluating the long-term durability of VC^3 mortars, including resistance to carbonation, sulfate attack, chloride ingress, swelling, and shrinkage assessment to further validate their sustainability for practical applications, as these properties require an entirely distinct testing matrix and extensive standalone evaluation.

Funding

This work was co-funded by the European Commission Horizon Europe research and innovation programme [Grant Agreement No 101123293], (SINCERE- The Second Life of Modern Period Architecture: Resilient and Adaptive Renovation towards Net-Zero Carbon Heritage Buildings); and by Gobierno de Navarra [Grant Number PC24-007-004 ECO-HEAT].

CRediT authorship contribution statement

Mohammad Hossein Nofalah: Conceptualization, Data curation, Formal analysis, Investigation, Methodology, Visualization, Writing – original draft. **Loucas Kyriakou:** Conceptualization, Investigation, Writing – review & editing. **José María Fernández:** Conceptualization, Resources, Writing – review & editing. **Íñigo Navarro-Blasco:** Conceptualization, Data curation, Funding acquisition, Methodology, Project administration, Resources, Supervision. **José Ignacio Álvarez:** Conceptualization, Funding acquisition, Project administration, Resources, Supervision, Writing – review & editing.

Declaration of competing interest

The authors declare that they have no conflict of interest.

Acknowledgements

The authors express their gratitude for the technical support provided by Cristina Luzuriaga and Marta Yárnoz Martín.

Appendix A. Supplementary data

Supplementary data to this article can be found online at https://doi.org/10.1016/j.jobe.2026.116654.

Data availability

Data will be made available on request.

References

[1] E. Gartner, Industrially interesting approaches to “low-CO2” cements, Cement Concr. Res. 34 (2004) 1489–1498, https://doi.org/10.1016/j.cemconres.2004.01.021.
[2] J.B. Martin, Carbonate minerals in the global carbon cycle, Chem. Geol. 449 (2017) 58–72, https://doi.org/10.1016/j.chemgeo.2016.11.029.
[3] L. Barcelo, J. Kline, G. Walenta, E. Gartner, Cement and carbon emissions, Mater. Struct. 47 (2014) 1055–1065, https://doi.org/10.1617/s11527-013-0114-5.
[4] S.A. Miller, V.M. John, S.A. Pacca, A. Horvath, Carbon dioxide reduction potential in the global cement industry by 2050, Cement Concr. Res. 114 (2018) 115–124, https://doi.org/10.1016/j.cemconres.2017.08.026.
[5] D. Zhao, J.M. Williams, P. Hou, A.J. Moment, S. Kawashima, Stabilizing mechanisms of metastable vaterite in cement systems, Cement Concr. Res. 178 (2024) 107441, https://doi.org/10.1016/j.cemconres.2024.107441.
[6] K.M.A. Hossain, Blended cement using volcanic ash and pumice, Cement Concr. Res. 33 (2003) 1601–1605, https://doi.org/10.1016/S0008-8846(03)00127-3.

[7] B. Li, L. Li, Y. He, B. He, D. Guo, Q. Nong, et al., Application of tuff powder in ultra-high performance concrete hardened in extreme plateau condition, Constr. Build. Mater. 474 (2025) 141185, https://doi.org/10.1016/j.conbuildmat.2025.141185.

[8] K.E. Seto, C.J. Churchill, D.K. Panesar, Influence of fly ash allocation approaches on the life cycle assessment of cement-based materials, J. Clean. Prod. 157 (2017) 65–75, https://doi.org/10.1016/j.jclepro.2017.04.093.

[9] K.-L. Lin, W.-T. Lin, S.-C. Chen, A. Sprince, Study on the cementation and engineering properties of ternary eco-binder mortar containing pulverized coal fly ash mixed with circulating fluidized bed co-fired fly ash, J. CO2 Util. 83 (2024) 102787, https://doi.org/10.1016/j.jcou.2024.102787.

[10] B. Ali, MH El Ouni, R. Kurda, Life cycle assessment (LCA) of precast concrete blocks utilizing ground granulated blast furnace slag, Environ. Sci. Pollut. Control Ser. 29 (2022) 83580–83595, https://doi.org/10.1007/s11356-022-21570-7.

[11] L. Xu, J. Wang, K. Li, T. Hao, Z. Li, L. Li, et al., New insights on dehydration at elevated temperature and rehydration of GGBS blended cement, Cem. Concr. Compos. 139 (2023) 105068, https://doi.org/10.1016/j.cemconcomp.2023.105068.

[12] B. Lothenbach, K. Scrivener, R.D. Hooton, Supplementary cementitious materials, Cement Concr. Res. 41 (2011) 1244–1256, https://doi.org/10.1016/j.cemconres.2010.12.001.

[13] A. Gholizadeh-Vayghan, M.-H. Nofallah, A. Khaloo, Technoeconomic study of alkali-activated slag concrete with a focus on strength, CO2 emission, and material cost, J. Mater. Civ. Eng. 33 (2021), https://doi.org/10.1061/(ASCE)MT.1943-5533.0003763.

[14] M.-H. Nofalah, P. Ghadir, H. Hasanzadehshooiili, M. Aminpour, A.A. Javadi, M. Nazem, Effects of binder proportion and curing condition on the mechanical characteristics of volcanic ash- and slag-based geopolymer mortars; machine learning integrated experimental study, Constr. Build. Mater. 395 (2023) 132330, https://doi.org/10.1016/j.conbuildmat.2023.132330.

[15] R. Snellings, P. Suraneni, J. Skibsted, Future and emerging supplementary cementitious materials, Cement Concr. Res. 171 (2023) 107199, https://doi.org/10.1016/j.cemconres.2023.107199.

[16] R. Snellings, A. Machner, G. Bolte, H. Kamyab, P. Durdzinski, P. Teck, et al., Hydration kinetics of ternary slag-limestone cements: impact of water to binder ratio and curing temperature, Cement Concr. Res. 151 (2022) 106647, https://doi.org/10.1016/j.cemconres.2021.106647.

[17] Y. Wang, L. Lei, C. Shi, Effect of diethanolisopropanolamine and ethyldiisopropylamine on hydration and strength development of cement-fly ash-limestone ternary blend, Cem. Concr. Compos. 145 (2024) 105354, https://doi.org/10.1016/j.cemconcomp.2023.105354.

[18] J. Lee, B. Lothenbach, J. Moon, Performance improvement of Portland-limestone cement by mechanochemical activation, Cement Concr. Res. 176 (2024) 107411, https://doi.org/10.1016/j.cemconres.2023.107411.

[19] L. Li, M. Cao, H. Yin, Comparative roles between aragonite and calcite calcium carbonate whiskers in the hydration and strength of cement paste, Cem. Concr. Compos. 104 (2019) 103350, https://doi.org/10.1016/j.cemconcomp.2019.103350.

[20] W. Zhang, J. Wang, Z. Chen, Hydration kinetics, strength, autogenous shrinkage, and sustainability of cement pastes incorporating ultrafine limestone powder, Case Stud. Constr. Mater. 20 (2024) e03149, https://doi.org/10.1016/j.cscm.2024.e03149.

[21] J. Sun, F. Zunino, K. Scrivener, Hydration and phase assemblage of limestone calcined clay cements (LC3) with clinker content below 50 %, Cement Concr. Res. 177 (2024) 107417 https://doi.org/10.1016/j.cemconres.2023.107417.

[22] Y. Li, Y. Li, H. Ma, J. Li, The hydration, microstructure, and mechanical properties of vaterite calcined clay cement (VC3), Cement Concr. Res. 175 (2024) 107374, https://doi.org/10.1016/j.cemconres.2023.107374.

[23] K. Scrivener, F. Avet, H. Maraghechi, F. Zunino, J. Ston, W. Hanpongpun, et al., Impacting factors and properties of limestone calcined clay cements (LC ^{3}), Green Mater. 7 (2019) 3–14, https://doi.org/10.1680/jgrma.18.00029.

[24] M. Antoni, J. Rossen, F. Martirena, K. Scrivener, Cement substitution by a combination of metakaolin and limestone, Cement Concr. Res. 42 (2012) 1579–1589, https://doi.org/10.1016/j.cemconres.2012.09.006.

[25] H. Mehdizadeh, T.-C. Ling, Hydration and strength of cement paste containing metastable vaterite derived from recycled concrete fines and CO2, Cement Concr. Res. 194 (2025) 107891, https://doi.org/10.1016/j.cemconres.2025.107891.

[26] H. Mehdizadeh, K.H. Mo, T.-C. Ling, CO2-fixing and recovery of high-purity vaterite CaCO3 from recycled concrete fines, Resour. Conserv. Recycl. 188 (2023) 106695, https://doi.org/10.1016/j.resconrec.2022.106695.

[27] Q. Song, M.-Z. Guo, T.-C. Ling, Synthesis of high-purity and stable vaterite via leaching–carbonation of basic oxygen furnace slag, ACS Sustain. Chem. Eng. 12 (2024) 4081–4091, https://doi.org/10.1021/acssuschemeng.3c07375.

[28] T. Beuvier, B. Calvignac, G.J.-R. Delcroix, M.K. Tran, S. Kodjikian, N. Delorme, et al., Synthesis of hollow vaterite CaCO3 microspheres in supercritical carbon dioxide medium, J. Mater. Chem. 21 (2011) 9757, https://doi.org/10.1039/c1jm10770d.

[29] B. Lu, Y. Zhou, L. Jiang, Z. Liu, G. Hou, High-purity vaterite CaCO3 recovery through wet carbonation of magnesium slag and leaching residue utilization in cement, Cem. Concr. Compos. 145 (2024) 105353, https://doi.org/10.1016/j.cemconcomp.2023.105353.

[30] C.W. Hargis, I.A. Chen, M. Devenney, M.J. Fernandez, R.J. Gilliam, R.P. Thatcher, Calcium carbonate cement: a carbon capture, utilization, and storage (CCUS) technique, Materials 14 (2021) 2709, https://doi.org/10.3390/ma14112709.

[31] C.W. Hargis, A. Telesca, P.J.M. Monteiro, Calcium sulfoaluminate (Ye'elimite) hydration in the presence of gypsum, calcite, and vaterite, Cement Concr. Res. 65 (2014) 15–20, https://doi.org/10.1016/j.cemconres.2014.07.004.

[32] F. Wu, J. Qin, Y. Cao, J. Yang, L. Jiang, B. Lu, et al., Effects of vaterite and leachate solid residue prepared from magnesium slag on the performance of cement mortar, Constr. Build. Mater. 429 (2024) 136409, https://doi.org/10.1016/j.conbuildmat.2024.136409.

[33] European Committee for Standardization, Methods of Testing Cement. Part 1: Determination of Strength, 2018. UNE-EN 196-1. Brussels, Belgium.

[34] M.H. Nofalah, L. Kyriakou, J.M. Fernández, Í. Navarro-Blasco, J.I. Álvarez, The Use of Vaterite in Calcined Clay Cement Binders for Sustainable Production, 2026, pp. 65–73, https://doi.org/10.1007/978-981-95-1818-0_8.

[35] Y. Mori, T. Enomae, A. Isogai, Preparation of pure vaterite by simple mechanical mixing of two aqueous salt solutions, Mater. Sci. Eng. C 29 (2009) 1409–1414, https://doi.org/10.1016/j.msec.2008.11.009.

[36] Q. Shen, H. Wei, Y. Zhou, Y. Huang, H. Yang, D. Wang, et al., Properties of amorphous calcium carbonate and the template action of vaterite spheres, J. Phys. Chem. B 110 (2006) 2994–3000, https://doi.org/10.1021/jp055063o.

[37] S. Kim, J. Jeon, M.-J. Kim, Vaterite production and particle size and shape control using seawater as an indirect carbonation solvent, J. Environ. Chem. Eng. 10 (2022) 107296, https://doi.org/10.1016/j.jece.2022.107296.

[38] A. Rubio-Aguinaga, L. Kyriakou, J.M. Fernández, Í. Navarro-Blasco, J.I. Álvarez, Microstructural analysis of bio-based PCM-enhanced lime mortars: durability and energy efficiency for sustainable buildings, Constr. Build. Mater. 481 (2025) 141569, https://doi.org/10.1016/j.conbuildmat.2025.141569.

[39] A. Rubio-Aguinaga, J.M. Fernández, Í. Navarro-Blasco, J.I. Álvarez, Air lime renders with microencapsulated phase change materials: assessment of microstructural and thermal properties, Constr. Build. Mater. 452 (2024) 138862, https://doi.org/10.1016/j.conbuildmat.2024.138862.

[40] European Committee for Standardization, Methods of test for mortar for masonry, in: Part 3: Determination of Consistence of Fresh Mortar (By Flow Table) UNE-EN 1015-3. Brussels, Belgium, 2006.

[41] European Committee for Standardization, Methods of Test for Mortar for Masonry - Part 9: Determination of Workable Life and Correction Time of Fresh Mortar UNE-EN 1015-9, 2000. Brussels, Belgium.

[42] ASTM International, Standard Test Method for Compressive Strength of Cylindrical Concrete Specimens, C39/C39M, ASTM, West Conshohocken, 2016.

[43] R.G. Pillai, R. Gettu, M. Santhanam, S. Rengaraju, Y. Dhandapani, S. Rathnarajan, et al., Service life and life cycle assessment of reinforced concrete systems with limestone calcined clay cement (LC3), Cement Concr. Res. 118 (2019) 111–119, https://doi.org/10.1016/j.cemconres.2018.11.019.

[44] E. Qoku, T.A. Bier, G. Schmidt, J. Skibsted, Impact of sulphate source on the hydration of ternary pastes of Portland cement, calcium aluminate cement and calcium sulphate, Cem. Concr. Compos. 131 (2022) 104502, https://doi.org/10.1016/j.cemconcomp.2022.104502.

[45] K. Scrivener, R. Snellings, B. Lothenbach (Eds.), A Practical Guide to Microstructural Analysis of Cementitious Materials, CRC Press, 2018, https://doi.org/10.1201/b19074.

[46] Y.A. Al-Noaimat, M. Chougan, M.J. Al-kheetan, O. Al-Mandhari, W. Al-Saidi, M. Al-Maqbali, et al., 3D printing of limestone-calcined clay cement: a review of its potential implementation in the construction industry, Results Eng. 18 (2023) 101115, https://doi.org/10.1016/j.rineng.2023.101115.

[47] D. Zhao, J.M. Williams, A.-H.A. Park, S. Kawashima, Rheology of cement pastes with calcium carbonate polymorphs, Cement Concr. Res. 172 (2023) 107214, https://doi.org/10.1016/j.cemconres.2023.107214.
[48] A. Baranyi, K. Kopecskó, L. Csetényi, Assessing setting times of cementitious materials using semi-adiabatic calorimetry, J. Therm. Anal. Calorim. 149 (2024) 9193–9201, https://doi.org/10.1007/s10973-024-13375-2.
[49] Practice for measuring hydration kinetics of hydraulic cementitious mixtures using isothermal calorimetry. https://doi.org/10.1520/C1679-17, 2017.
[50] M.H. Nofalah, L. Kyriakou, J.M. Fernández, Í. Navarro-Blasco, J.I. Álvarez, Impact of vaterite integration on the hydration, microstructure and performance of calcined clay cements, Sci. Rep. (2026), https://doi.org/10.1038/s41598-026-51241-3.
[51] D. Jansen, Ch Naber, D. Ectors, Z. Lu, X.-M. Kong, F. Goetz-Neunhoeffer, et al., The early hydration of OPC investigated by in-situ XRD, heat flow calorimetry, pore water analysis and 1H NMR: learning about adsorbed ions from a complete mass balance approach, Cement Concr. Res. 109 (2018) 230–242, https://doi.org/10.1016/j.cemconres.2018.04.017.
[52] R. Snellings, A. Bazzoni, K. Scrivener, The existence of amorphous phase in Portland cements: physical factors affecting rietveld quantitative phase analysis, Cement Concr. Res. 59 (2014) 139–146, https://doi.org/10.1016/j.cemconres.2014.03.002.
[53] F. Zunino, K. Scrivener, Hydration and strength development of low-clinker (<50 %) factor limestone calcined clay cements (LC3): a comparative study with natural pozzolans, Constr. Build. Mater. 499 (2025) 144075, https://doi.org/10.1016/j.conbuildmat.2025.144075.
[54] E. Gallucci, K. Scrivener, Crystallisation of calcium hydroxide in early age model and ordinary cementitious systems, Cement Concr. Res. 37 (2007) 492–501, https://doi.org/10.1016/j.cemconres.2007.01.001.
[55] X. Chen, S. Wei, Q. Wang, M. Tang, X. Shen, X. Zou, et al., Morphology prediction of portlandite: atomistic simulations and experimental research, Appl. Surf. Sci. 502 (2020) 144296, https://doi.org/10.1016/j.apsusc.2019.144296.